Exhumation of the Main Central Thrust from Lower Crustal Depths, Eastern Bhutan Himalaya

C. G. DANIEL[1],*, L. S. HOLLISTER[1], R. R. PARRISH[2] AND D. GRUJIC[3]

[1]*Department of Geosciences, Princeton University, Princeton, NJ 08542, USA (cdaniel@bucknell.edu)*
[2]*Department of Geology, University of Leicester & NERC Isotope Geosciences Laboratory, British Geological Survey, Keyworth, Notts, NG12 5GG UK*
[3]*Department of Earth Sciences, Dalhousie University, Halifax, NS B3H 3J5, Canada*

ABSTRACT   Geothermometry and mineral assemblages show an increase of temperature structurally upwards across the Main Central Thrust (MCT); however, peak metamorphic pressures are similar across the boundary, and correspond to depths of 35–45 km. Garnet-bearing samples from the uppermost Lesser Himalayan sequence (LHS) yield metamorphic conditions of 650–675 °C and 9–13 kbar. Staurolite-kyanite schists, about 30 m above the MCT, yield *P-T* conditions near 650 °C, 8–10 kbar. Kyanite-bearing migmatites from the Greater Himalayan sequence (GHS) yield pressures of 10–14 kbar at 750–800 °C. Top-to-the-south shearing is synchronous with, and postdates peak metamorphic mineral growth.

Metamorphic monazite from a deformed and metamorphosed Proterozoic gneiss within the upper LHS yield U/Pb ages of 20–18 Ma. Staurolite-kyanite schists within the GHS, a few metres above the MCT, yield monazite ages of *c.* 22 ± 1 Ma. We interpret these ages to reflect that prograde metamorphism and deformation within the Main Central Thrust Zone (MCTZ) was underway by *c.* 23 Ma. U/Pb crystallization ages of monazite and xenotime in a deformed kyanite-bearing leucogranite and kyanite-garnet migmatites about 2 km above the MCT suggest crystallization of partial melts at 18–16 Ma. Higher in the hanging wall, south-verging shear bands filled with leucogranite and pegmatite yield U/Pb crystallization ages for monazite and xenotime of 14–15 Ma, and a 1–2 km thick leucogranite sill is 13.4 ± 0.2 Ma. Thus, metamorphism, plutonism and deformation within the GHS continued until at least 13 Ma. *P-T* conditions at this time are estimated to be 500–600 °C and near 5 kbar. From these data we infer that the exhumation of the MCT zone from 35 to 45 km to around 18 km, occurred from 18 to 16 to *c.* 13 Ma, yielding an average exhumation rate of 3–9 mm year^{-1}. This process of exhumation may reflect the ductile extrusion (by channel flow) of the MCTZ from between the overlying Tibetan Plateau and the underthrusting Indian plate, coupled with rapid erosion.

Key words: Bhutan Himalaya; ductile extrusion; garnet zoning; thermobarometry; U/Pb geochronology.

INTRODUCTION

The Main Central Thrust (MCT) and the broad zone of shearing associated with it (the Main Central Thrust Zone, MCTZ) is one of the most fundamental structures within the Himalayan orogenic belt (Hodges, 2000; and references therein; Beaumont *et al.*, 2001). The MCT is commonly interpreted as a major intracontinental thrust associated with the Miocene exhumation of the high-grade, metamorphic core of the Himalayas during the India-Asia collision. At depth, the MCT is interpreted to merge with the Main Boundary Thrust (MBT) and the Main Frontal Thrust (MFT) to form a northward dipping decollement (Gansser, 1964; Schelling & Arita, 1991; Zhao *et al.*, 1993). The decollement extends 150–200 km to the north, dips 10–15° north, and reaches depths of

40–50 km (Hauck *et al.*, 1998). This decollement is referred to as the Himalayan Sole thrust (Hodges, 2000) or the Main Himalayan Thrust (MHT; Zhao *et al.*, 1993; Hauck *et al.*, 1998).

The zone of deformation, associated with the MCT, extends for about 2500 km along the strike of the orogen, and is hundreds of metres to several kilometres thick (Gansser, 1964; Hodges, 2000). The MCTZ dips shallowly north and records dominantly south-directed shearing across the length of the Himalaya (Gansser, 1964; Grujic *et al.*, 1996; Hubbard, 1996; Grasemann & Vannay, 1999; Hodges, 2000). Along the entire length of the Himalaya, an inverted metamorphic field gradient is also observed across the MCT, with greenschist to amphibolite facies metamorphic rocks in the footwall, and upper amphibolite to granulite facies rocks within the hanging wall (Heim & Gansser, 1939; LeFort, 1975; Hodges, 2000). Although considerable work has been done to document and understand the processes leading to this inverted metamorphic field gradient, the mechanisms are still much debated

* Now at: Department of Geology, Bucknell University, Lewisburg, PA 17837, USA (E-mail: cdaniel@bucknell.edu).

(Hubbard, 1989, 1996; Jain & Manickavasagam, 1993; Jamieson *et al.*, 1996; Harrison *et al.*, 1997, 1998; Vannay & Grasemann, 1998, 2001; Grasemann & Vannay, 1999; Vannay *et al.*, 1999; Hodges, 2000; Beaumont *et al.*, 2001; Kohn *et al.*, 2001).

Similar features characterize the MCTZ within the Kingdom of Bhutan (Gansser, 1983; Grujic *et al.*, 1996, 2002; Davidson *et al.*, 1997). Early work by Gansser (1983) defined the contact of the Lesser and Greater Himalayan sequences as the Main Central Thrust (MCT). However, he also noted that a broad zone of deformation extended both above and below this lithotectonic boundary. This broad zone of deformation is referred to as the Main Central Thrust Zone (MCTZ; Grujic *et al.*, 1996). Grujic *et al.* (1996, 2002) showed that penetrative top-to-the south thrust deformation within the MCTZ of Bhutan occurred at high temperature, and extends from approximately 2 km below the MCT, upwards through the entire Greater Himalayan sequence. Gansser (1983) also pointed out that metamorphic temperatures increased structurally upwards from the Lesser Himalayan sequence (LHS) to the Greater Himalayan sequence (GHS), consistent with the inverted metamorphic field gradient observed in other areas of the Himalayas.

Davidson *et al.* (1997) described mineral assemblage and compositional data for samples within the Greater Himalayan sequence of Bhutan. They concluded that the hanging wall of the Main Central Thrust had been exhumed rapidly from depths corresponding to > 8 kbar, to depths corresponding to about 5 kbar before cooling from peak metamorphic temperatures. They noted that one sample from the uppermost part of the LHS contained garnet with low-Ca cores and distinctly higher-Ca rims, suggesting a *P–T* and/or reaction history different than that in the overlying Greater Himalaya sequence.

In this paper we examine several samples from the uppermost part of the Lesser Himalayan sequence and from the overlying Greater Himalayan sequence in order to determine metamorphic *P-T* conditions, and to document any pressure and temperature field gradients across the MCT. A measurable break in pressure across the MCT would be consistent with significant thrusting and lateral displacement juxtaposing two significantly different structural levels across a discrete structure (the MCT). A hot iron effect on the footwall of the MCT (LeFort, 1975) by the hanging wall could be a consequence of this structural history. Alternatively, relatively uniform and high pressures across the MCT would be consistent with juxtaposition of the colder footwall and hotter hanging wall at depths corresponding to the peak metamorphic pressures. The observed metamorphic field gradient across the MCT would be a consequence of rapid exhumation that preserved a record of the thermal structure that had formed at depth.

We use detailed X-ray maps to document mineral zoning patterns, to interpret both prograde and retrograde mineral reactions, and to help identify appropriate mineral compositions for thermobarometry. Furthermore, U/Pb geochronology is used to determine the rate of exhumation of the hanging wall of the MCT, and to establish time constraints for the duration of metamorphism, plutonism, and deformation of both the hanging wall and footwall. Finally, we place our results in the context of a channel flow model proposed for Bhutan (Grujic *et al.*, 2002) and the Himalaya in general (Beaumont *et al.*, 2001).

TECTONOSTRATIGRAPHY

Several formations occur within the Lesser Himalayan sequence of Bhutan (Fig. 1). Immediately below the MCT is the Jaishidanda Formation (Fig. 1), characterized by garnet-bearing mica schists interlayered with quartzites and phyllites (Dasgupta, 1995). As defined by Dasgupta (1995), this unit varies in thickness from about 30–600 m, and extends continuously from westernmost Bhutan to east of the Kuru Chu gorge, where it appears to be structurally cut out by faulting.

Directly below the Jaishidanda Formation is the Shumar Formation (Dasgupta, 1995) or Daling-Shumar Group (Gansser, 1983; Fig. 1). This unit consists of interlayered quartzites and chlorite phyllites tectonically interleaved with lenses of granite and carbonates of the Baxa Formation. The granitic rocks have yielded Proterozoic crystallization ages (Thimm *et al.*, 1999). The granites are penetratively deformed and have tectonized borders, leading Ray *et al.* (1989), Dasgupta (1995), and Ray (1995) to conclude they are tectonic slivers of the basement. Alternatively, the granite bodies could represent intrusions into the continental margin sequence, which were later deformed in the India-Asia collision.

Following Gansser (1983), we divide the Greater Himalayan sequence into a gneissic unit, the Paro metasediments, and leucogranites. The gneissic unit immediately overlies the MCT; it is dominated by granitic orthogneisses, with cm-scale, K-feldspar porphyroclasts. Lesser amounts of paragneiss, marble, amphibolite and biotite-rich schists occur within this unit. The Paro metasedimentary unit is dominated by metacarbonates interlayered with schist and quartzite, and minor amounts of amphibolite. Migmatite, leucogranite and leucotonalite dykes and sills generally increase in abundance from around 500 m above the MCT, upwards towards the Kakhtang Thrust. The largest, map-scale plutons occur above the Kakhtang thrust (Fig. 1).

Overlying the crystalline rocks of the GHS are the Tethyan sedimentary units to the north, and the Chekha Formation across the central part of Bhutan. The South Tibetan Detachment system (STD) separates the Tethyan sedimentary rocks from the underlying GHS. A tectonic contact with top-to-the-north shear sense separates the Chekha Formation from the underlying GHS, and is interpreted as part of the South Tibetan Detachment (Edwards *et al.*, 1999; Grujic *et al.*, 2002). Garnet-staurolite schists occur at the base of the Chekha Formation (Grujic *et al.*, 2002) and the Tethyan sediments (Burchfiel *et al.*, 1992); however, metamorphic grade decreases sharply up section, such that unmetamorphosed sediments occur a few hundred metres above the contact with the GHS.

REGIONAL STRUCTURES

The Main Central Thrust

Excellent 3-D exposure of the MCT is found across the deep Kuru Chu gorge (Fig. 1) of eastern Bhutan. Two places were found where the MCT can be defined to within 1 m, near Shongar Dzong, and south-west of Tashigang. The MCT can be defined to within 10 m at Barsong, and along the western side of Kuru Chu, south-west of Lhuntse, and within 100 m along the Kuru Chu south of Lhuntse.
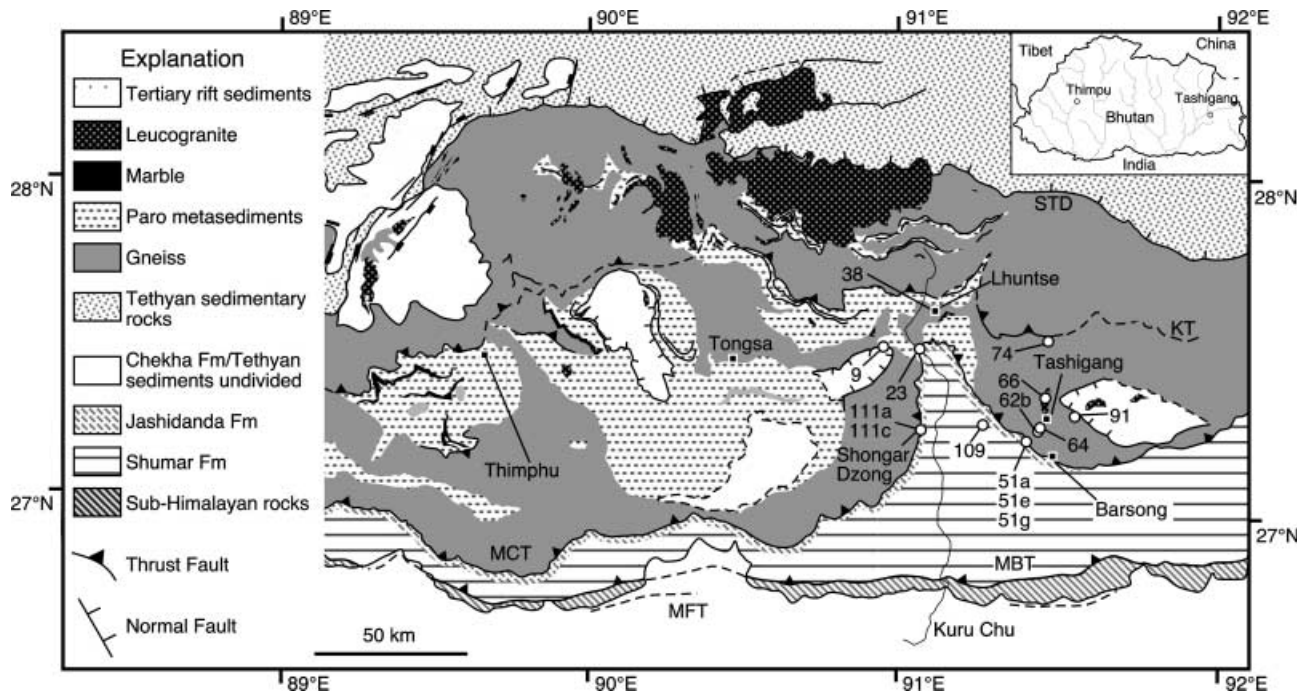
Fig. 1. Simplified geological map of Bhutan (modified from Gansser, 1983; Bhargava, 1995, plate 1; Edwards *et al.*, 1999) showing tectonostratigraphic units, sample locations, villages, and major structures: Main Frontal Thrust (MFT), Main Boundary Thrust (MBT), Main Central Thrust (MCT), Kakhtang Thrust (KT), and the South Tibetan Detachment (STD).

Our definition of the MCT in Bhutan follows that of Gansser (1983), and Davidson *et al.* (1997); it is in accord with that of Pêcher (1989) for Nepal. The trace of the MCT (Fig. 1) separates a thick, distinctive section of quartzite (the Shumar Formation) and phyllite/schist (the Jaishidanda Formation) from orthogneiss or biotite-rich schist of the Greater Himalayan sequence. This boundary closely coincides with the first occurrence of kyanite in the GHS. Where kyanite-bearing schist is observed below the augen gneiss (location 51), the MCT is placed at the kyanite-in isograd. Thus, the MCT corresponds to both a protolith and metamorphic boundary. In Bhutan, we observe a thick zone of penetrative shear across the MCT that begins at least 2 km structurally below the MCT, and continues up through the entire GHS to the South Tibetan Detachment (Grujic *et al.*, 2002). This zone of penetrative shear corresponds to the 'MCT zone'. Strain gradients are observed within this zone, however, in general, strain decreases moving away from the MCT.

Kakhtang Thrust

A second major thrust, the Kakhtang thrust, occurs above the MCT and nearly doubles the thickness of the Greater Himalayan sequence in Bhutan (Grujic *et al.*, 1996, 2002; Davidson *et al.*, 1997). The Kakhtang thrust cuts across regional foliation and metamorphic isograds and is interpreted as an out-of-sequence thrust (Grujic *et al.*, 1996, 2002; Davidson *et al.*, 1997). Sillimanite-bearing migmatite and the largest bodies of leucogranite in Bhutan occur in the hanging wall of the Kakhtang thrust (Dietrich & Gansser, 1981; Gansser, 1983; Swapp & Hollister, 1991; Davidson *et al.*, 1997).

South Tibetan Detachment

The South Tibetan Detachment (STD) roughly parallels the MCT and extends nearly the entire length of the Himalaya (Burchfiel *et al.*, 1992; Hodges, 2000; Edwards *et al.*, 1996, 1999; Wu *et al.*, 1998). In Bhutan (Fig. 1), this shear zone dips moderately to steeply north, shows top-to-the-north (normal) shear sense, and separates the GHS

Table 1. Major silicate minerals.*

	Chl	Grt	St	Ky	Sil	Pl	Leucosome
Chekha Formation							
9 (+8 km**)	x	x			x		
Greater Himalayan samples							
38 (+2 km)		x		x	x	x	x
74 (+20 km)	r	x	t	x	x	x	x
62b (+2 km)	r	x	t	x	t	x	x
23 (+500 m)		x		x	t	x	x
51g (+30 m)	r	x	x	x		x	
Lesser Himalayan samples							
51a (−10 m)	r	x					
51e (−1 m)	r	x				x	
111a (−20 m)		x				x	
111c (−20 m)		x				x	

* all samples contain quartz, biotite, muscovite; r = retrograde; t = trace amounts.
** approximate distance in kilometres or metres structurally above the MCT.

from overlying Tethyan sedimentary units (Burchfiel *et al.*, 1992; Edwards *et al.*, 1996, 1999). Grujic *et al.* (2002) proposed that the tectonic contact between the Chekha Formation and the GHS is part of the STD based upon top-to-the north shearing at the base of the Chekha Formation, and a break in metamorphic grade from migmatite in the GHS to garnet-staurolite bearing schist in the lowermost Chekha Formation (Table 1).

MINERAL ASSEMBLAGES AND DEFORMATION ACROSS THE MCT

We examined an approximately 20 km thick section beginning *c.* 500 m below the MCT and extending structurally up to the Kakhtang thrust in order to understand the relative timing of metamorphism, partial melting and deformation. The mappable sequence of metamorphic zones is parallel to the MCT and includes, beginning

from below the MCT, (1) chlorite phyllite intercalated with quartzite, (2) garnet schist intercalated with quartzite (Jaishidanda Formation); continuing above the MCT, the sequence is (3) highly deformed staurolite-garnet-kyanite schist, (4) kyanite-garnet migmatite, (5) kyanite-sillimanite gneiss accompanied by sills and dykes of leucogranite, leucotonalite and pegmatite and (6) the Kakhtang thrust. This work focuses on the rocks within and above the garnet zone, up to the Kakhtang thrust. Major silicate mineral assemblages are summarized in Table 1.

Garnet Zone

Small garnet crystals (< 2 mm diameter) occur in the schist layers within the Jaishidanda Formation. This garnet typically contains cores with sigmoidal to spiral inclusion trails (Fig. 2a) and thin inclusion-free rims. The curved and spiral inclusion patterns may represent syn-tectonic growth during shearing across the MCTZ. Alternatively, the inclusions trails may represent intertectonic growth over a preexisting crenulation cleavage (Passchier & Trouw, 1996). The matrix consists of muscovite, biotite, quartz, plagioclase and opaques. Several samples show significant retrograde replacement of garnet by chlorite (Fig. 2b).

Below the MCT, quartzites, schists and phyllites are tightly folded, with axial planes subparallel to the main foliation, and the MCT. The fold axes are generally subparallel to the stretching lineations in the hanging-wall gneiss and schist. The quartzite retains bedding and right-side-up cross beds. Fabric analysis of the quartzite indicates dynamic recrystallization during top-to-the south shearing (Grujic *et al.*, 1996). The interlayered schists and phyllites contain shear bands (Fig. 2b,c) and mica fish indicating top-to-the-south shearing that overprints garnet growth. Dynamic recrystallization of feldspar indicates that deformation occurred at 400 °C (FitzGerald & Stünitz, 1993). Chlorite pseudomorphs of garnet are not deformed, and, thus, postdate the penetrative shearing (Fig. 2b). Peak metamorphic mineral assemblages are interpreted to be garnet + biotite + muscovite + plagioclase + quartz.

Staurolite–kyanite zone

Where biotite schist occurs for the first few tens of metres above the MCT, it contains garnet, staurolite, kyanite, muscovite, quartz and opaques with traces of sillimanite and retrograde chlorite. Most staurolite and garnet grains are subhedral or anhedral fragments containing straight inclusion trails that are discontinuous and oblique to the surrounding foliation (Fig. 2d). Some outer portions of garnet are clear of inclusions. Kyanite occurs as small, deformed grains in the matrix (Fig. 2d). Traces of sillimanite occur within the foliation plane. More commonly, orthogneiss occurs just above the MCT and shows a pronounced north trending, stretching lineation; σ-type porphyroclasts of K-feldspar indicate top-to-the-south shearing. The dynamic recrystallization of feldspar is consistent with temperatures > 400 °C during deformation (FitzGerald & Stünitz, 1993). Where biotite schist is at the protolith boundary, the schistosity is pronounced and parallel to the MCT; shear bands are abundant and all indicate top-to-the-south shearing after peak metamorphic conditions. Recrystallized biotite in the shear bands indicates that this deformation was above 350–400 °C, consistent with the quartz deformation fabrics described by Grujic *et al.* (1996). The peak metamorphic mineral assemblage in this sample is not clear. The occurrence of anhedral, embayed staurolite coexisting with kyanite suggests temperatures above the reaction staurolite + chlorite $\leftrightarrow$ Al_2SiO_5 + biotite + H_2O. However, the clear rims on several garnet suggest a second generation of garnet growth possibly by the higher temperature reaction staurolite + muscovite $\leftrightarrow$ garnet + Al_2SiO_5 + biotite.

Kyanite-migmatite zone

Kyanite-garnet migmatite and kyanite-bearing leucogranite veins and pods appear *c.* 500 m above the MCT and continue up

(20–25 km) to the Kakhtang thrust. Melt pods are concordant to foliation, are deformed within it, and are up to 5 cm thick (Fig. 3a). Kyanite crystals within these leucogranite pods and veins are preferentially aligned and define a N-trending mineral lineation. Partially melted metasediments contain kyanite-garnet-plagioclase-muscovite-biotite-quartz, opaques and rare to abundant sillimanite. Kyanite varies in length from a few mm up to 5 cm, and is typically kinked, fractured, or pulled apart (Fig. 2e). Plagioclase and quartz occur within pressure shadows around garnet. Coarse biotite and muscovite lie within the foliation. The kyanite-bearing leucosomes require *P-T* conditions > 8 kbar, and near 700 °C (Davidson *et al.*, 1997; Spear *et al.*, 1999); significant deformation postdates the crystallization of these migmatites.

Higher in the section, leucotonalitic leucosomes fills pressure shadows around garnet crystals (Fig. 3b). Plagioclase is about twice as abundant as quartz, and the symmetry of the pressure shadows is consistent with pure shear. Kyanite occurs as inclusions within garnet (Fig. 2f), and in the matrix. Sillimanite replacing kyanite (Fig. 2g) is consistent with decompression and/or heating into the sillimanite stability field. The fractured and boudinaged kyanite (Fig. 2e), leucosome-filled pressure shadows around garnet (Fig. 3b), and fractured garnet (Fig. 2f) are all consistent with a pure shear component to the deformation. These observations are consistent with evidence for flattening based upon previous work in Bhutan by Grujic *et al.* (1996) and in the western Himalayas by Grasemann *et al.* (1999). Open upright folds of the dominant foliation and slight bending of some kyanite grains suggests a component of late N-S shortening.

Leucogranites

Multiple generations of leucogranite (Davidson *et al.*, 1997) sills and dykes are observed about 2 km and higher above the MCT. The earliest intrusions are now concordant with foliation and are deformed into asymmetric to symmetric boudins (Fig. 3a). These sills and the foliation are cut by later generations of dykes that are folded with axial planes parallel to the foliation. The last generations of dykes crosscut the foliation and the earlier generations of leucogranite. Where multiple generations of leucogranite sills, dykes and veins occur, sillimanite and fibrolite are more abundant relative to kyanite. A large 2–3 km thick leucogranite sill occurs just north of Tashigang (Fig. 1). Leucosome-filled shear bands south of the Kakhtang thrust show top-to-the-south kinematics (Fig. 3c) and conjugate shear bands in gneiss (Fig. 3d) show pure shear while melt is present. East of Tashigang, along strike of the sill complex, but above it, bent kyanite blades are partially replaced by sillimanite (Fig. 2g).

Summary

Samples from all of the metamorphic zones show that top-to-the-south shearing was synchronous with, or postdates peak metamorphism. The GHS and lower Chekha Fm. also show evidence for a component of pure shear and top-to-the-north shearing (Fig. 2h) that was synchronous with or postdates the top-to-the-south shearing. The preservation of leucosome-filled pressure shadows with weakly deformed to undeformed quartz and feldspar (Fig. 3b), and of leucosome-filled conjugate shear bands (Fig. 3d) implies the presence of melt during pure shear deformation (Hand & Dirks, 1992). Thus, the final solidification of melt postdates penetrative top-to-the-south thrusting within the central part of the MCT. The increase in abundance of sillimanite, and of sillimanite partially replacing kyanite at higher structural levels in the GHS is consistent with either heating or decompression from the kyanite stability field to the sillimanite stability field.

MINERAL CHEMISTRY, ZONING PATTERNS AND INTERPRETATIONS

Mineral compositional data were collected with a Cameca SX 50 microprobe at Princeton University.
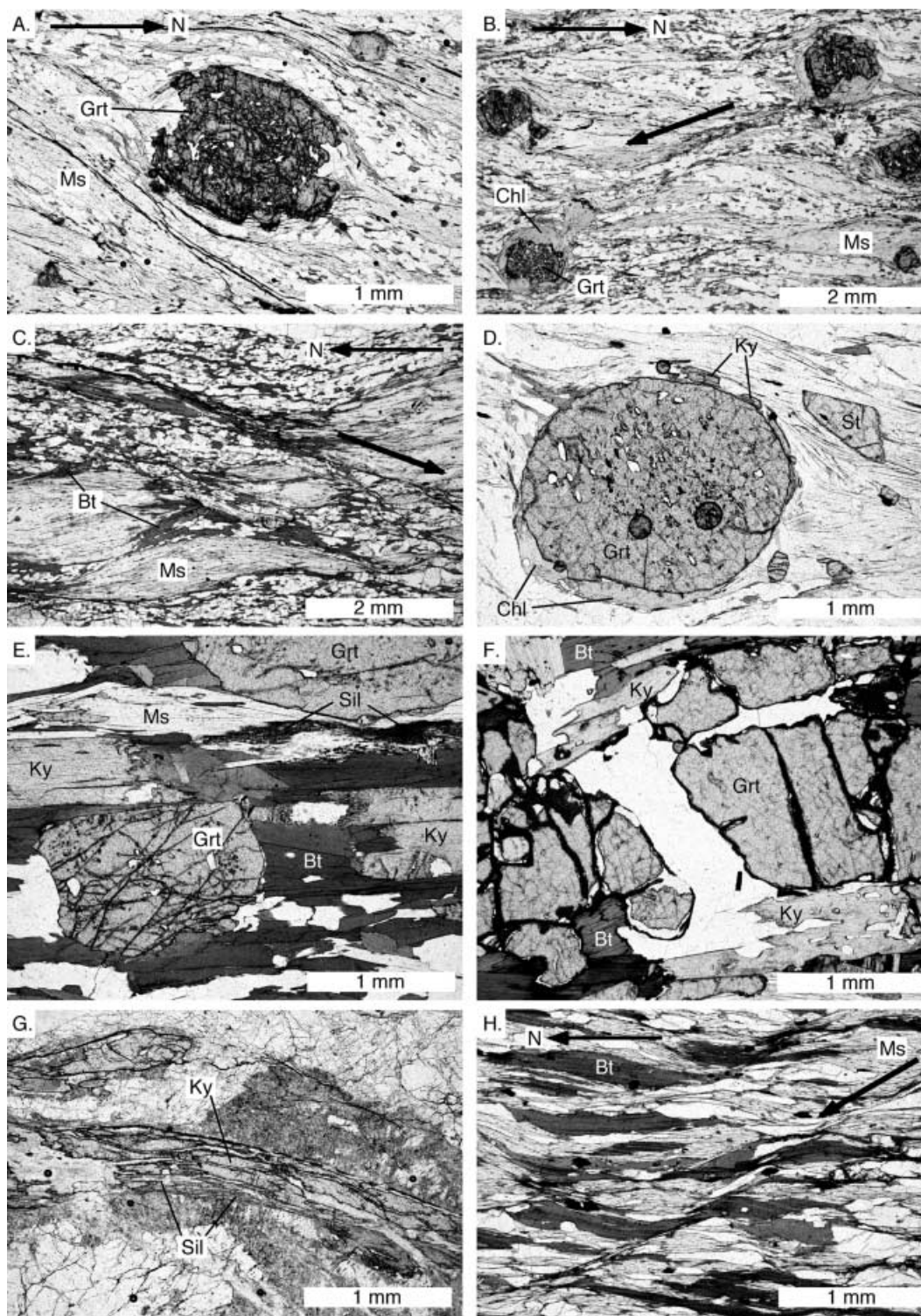
Fig. 2. Photomicrographs taken in plane-polarized light. All sections are cut parallel to the mineral lineation and perpendicular to foliation. (a) Garnet with spiral inclusion trails and pressure shadows, sample 51a. Inclusion trails are consistent with top-to-the-north shear during garnet growth. Top-to-the-south shear bands observed in matrix and adjacent samples. (b) Top-to-the-south shear bands and chlorite pseudomorph after garnet, sample 51e. (c) Top-to-the-south shear bands in sample 111. (d) Garnet, kyanite and staurolite, sample 51 g. Inclusion trails within garnet are straight and discontinuous with the matrix foliation. (e) Bent and broken kyanite laths adjacent to garnet; kyanite defines north-trending mineral lineation, traces of sillimanite replacing kyanite, sample 62b. (f) Kyanite inclusions within fractured garnet, sample 38. (g) Sillimanite partially replacing kyanite, sample 91. (h) Top-to-the-north shear bands in muscovite-biotite-quartz-plagioclase schist, sample 9.
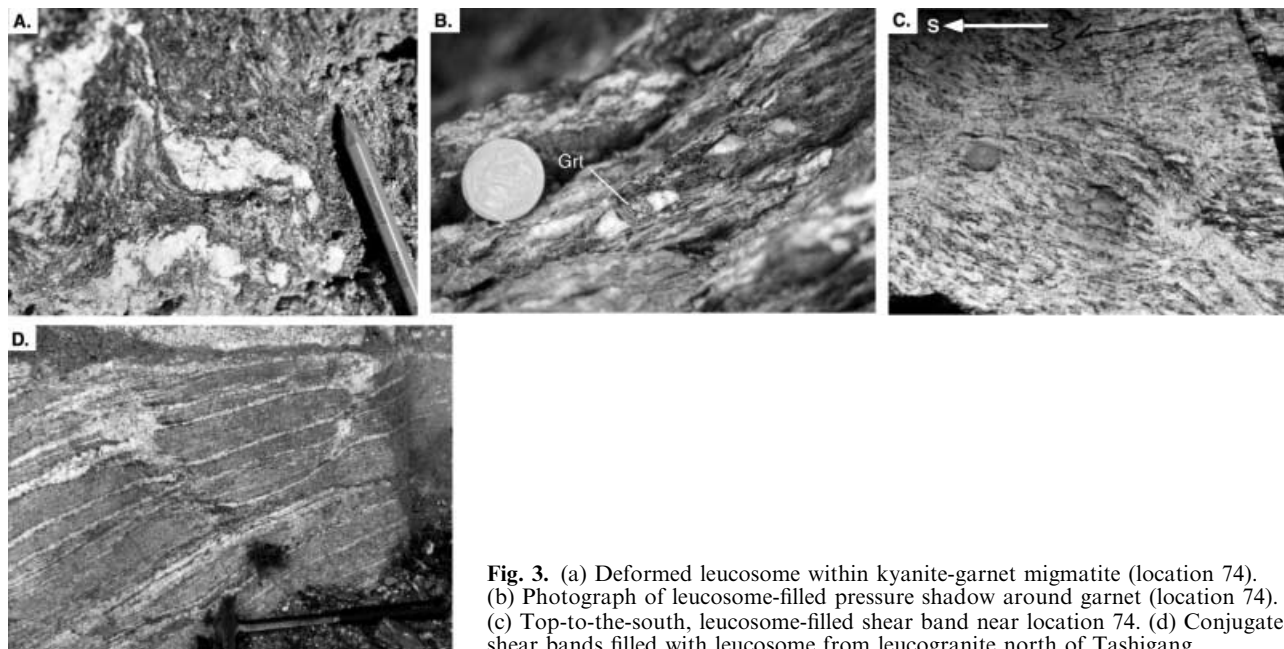
Fig. 3. (a) Deformed leucosome within kyanite-garnet migmatite (location 74). (b) Photograph of leucosome-filled pressure shadow around garnet (location 74). (c) Top-to-the-south, leucosome-filled shear band near location 74. (d) Conjugate shear bands filled with leucosome from leucogranite north of Tashigang.

Operating conditions were 15 kV, 20 nA and a beam size of 1–10 μm. Large area and detailed two dimensional X-ray maps were collected for all samples to characterize mineral zoning patterns (Figs 4–8). Multiple spot analyses were used to measure mineral compositions and to calibrate the X-ray maps. The X-ray maps were essential for identifying areas of garnet dissolution and diffusional reequilibration characterized by the truncation of Ca compositional zoning patterns, and reversals in Fe/(Fe + Mg) and Mn zoning trends at the garnet rim. The approximate elevations of the samples with respect to the MCT are given in Table 1. Mineral compositions keyed to the zoning maps are presented in Tables S2, S3, and S4.

Garnet zone

Garnet within the footwall of the MCT preserves growth-zoning patterns (Figs 4, 5 & 6). In sample 111a, Fe, Mg, and Mn zoning patterns are smooth and continuous from core to rim (Fig. 4). Fe/(Fe + Mg) decreases from 0.85 at the core to 0.81 near the rim. Local reversals of Fe/(Fe + Mg), up to 0.85, occur where the garnet rim is in contact with biotite. Mn decreases from $X_{Sps} = 0.21$ in the core to $X_{Sps} = 0.08$ near-rim, and locally increases again to $X_{Sps} = 0.14$ at the rim (Fig. 4). Ca shows a distinct break in zoning, with a low Ca core ($X_{Grs} = 0.01$) encompassed by a higher-Ca overgrowth ($X_{Grs} = 0.06$) that drops to $X_{Grs} = 0.02$ at the rim (Fig. 4). As observed in grossular map 2 (Fig. 4), the garnet core is fractured; however, the fractures do not continue into the higher-Grs rim. Nearly all garnet observed within this sample shows similar textures. We interpret these textures to

reflect an early garnet core of unknown age and infer a Miocene age for the overgrowth based upon metamorphic monazite ages from the region. Similar high-Ca overgrowths were observed in one additional sample (111c, discussed below) and were also documented by Davidson *et al.* (1997; sample 43).

Garnet zoning patterns within sample 111c are similar to 111a and, again, two generations of garnet appear to be present (Fig. 5). Several garnet show low Ca cores (Fig. 5, map 1) with higher-Ca overgrowths. However, one garnet within the sample was observed to have 'normal' Ca zoning that decreased from core to rim (Fig. 5, map 2). This garnet is interpreted to be second generation, and to have grown coincident with the higher-Ca overgrowth observed on other garnet crystals. Fe/Fe + Mg, Mn, and Ca all decrease smoothly from core to near-rim, and show zoning reversals in Fe/Fe + Mg and Mn at the garnet rim.

Garnet from sample 51e also preserves growth-zoning patterns (Fig. 6); however, deep embayments, truncations and pseudomorphs of chlorite indicate considerable garnet dissolution (Fig. 6, map 1). Rim compositions are more variable due to the differing amounts of dissolution. Fe/Fe + Mg decreases from about 0.90 in the core to 0.85 at the rim. X_{Sps} decreases from approximately 0.06 in the core to about 0.01 at the rim. Garnet from 51e does not show the high-Ca overgrowth observed in 111a, and 111c; instead, X_{Grs} decreases from about 0.15, in the core, to about 0.11 at the rim. No reversals in Fe/Fe + Mg or Mn were observed in the zoning maps.

Plagioclase is abundant in the matrix of 111a, 111c and 51e. Unfortunately, no plagioclase or mica
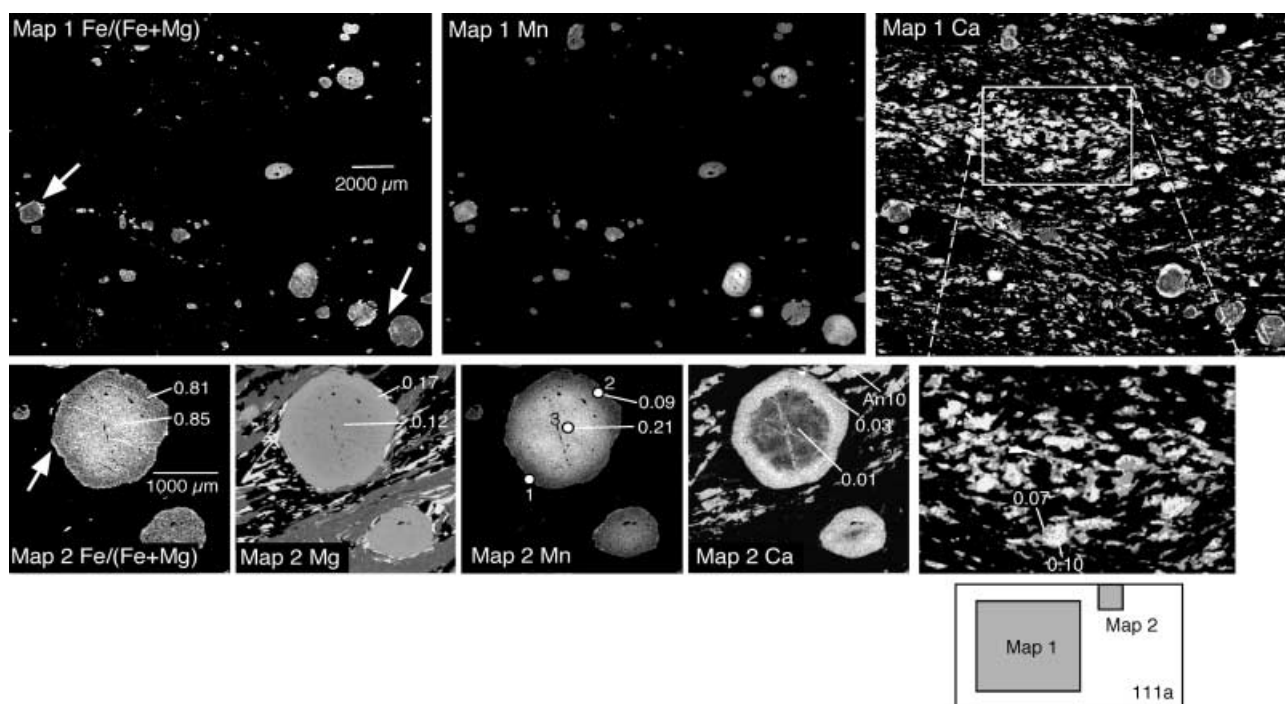
Fig. 4. X-ray maps from sample 111a showing compositional zoning patterns for garnet and plagioclase. Lighter shades indicate higher concentrations. Area enclosed by white box (map 1 Ca) is enlarged to show details of plagioclase zoning. Arrows indicate zoning reversals. Location of X-ray maps within the thin section is indicated by line drawing at centre right. Numbered points in map 2 Mn are keyed to analyses in Table 2. See text for interpretations and discussion. A colour version of this figure is available in the online version of the journal.
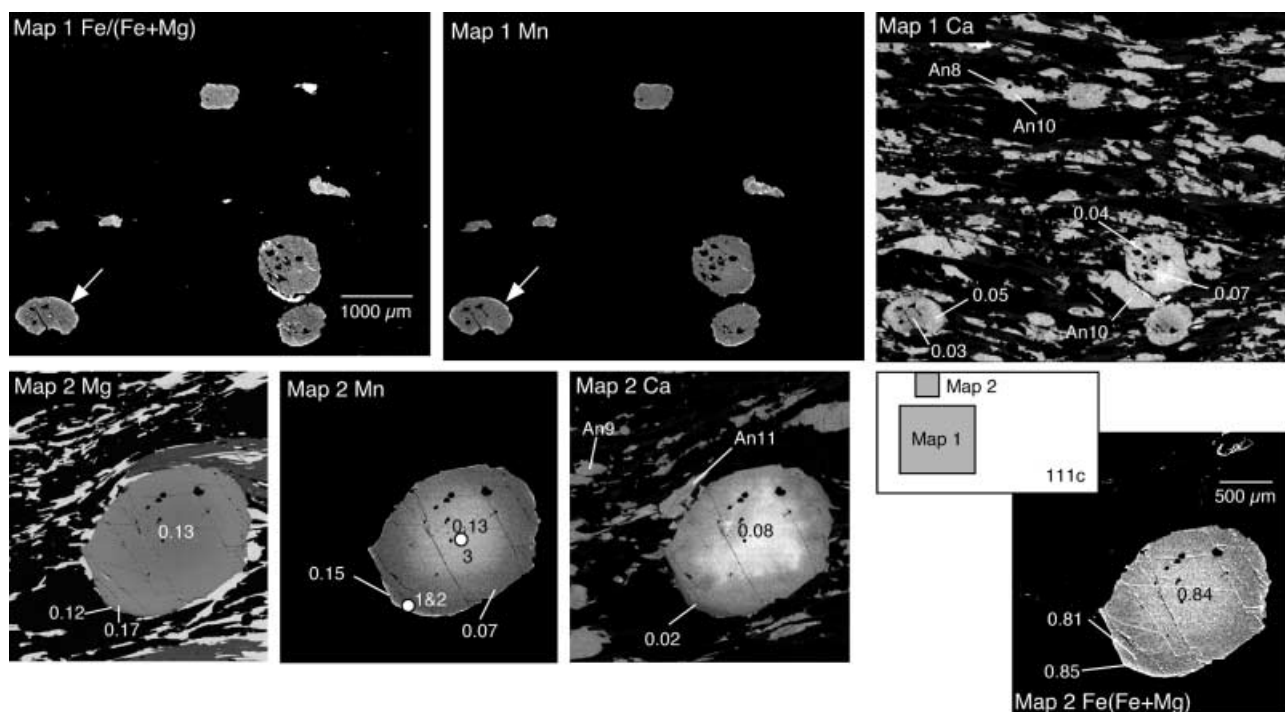
Fig. 5. X-ray maps from sample 111c showing compositional zoning patterns for garnet and plagioclase. Lighter shades indicate higher concentrations. Location of maps within the thin-section are shown in line drawing at centre right. Arrows indicate zoning reversals. Numbered points in map 2 Mn correspond to analyses in Table 2. See text for interpretations and discussion. A colour version of this figure is available in the online version of the journal.
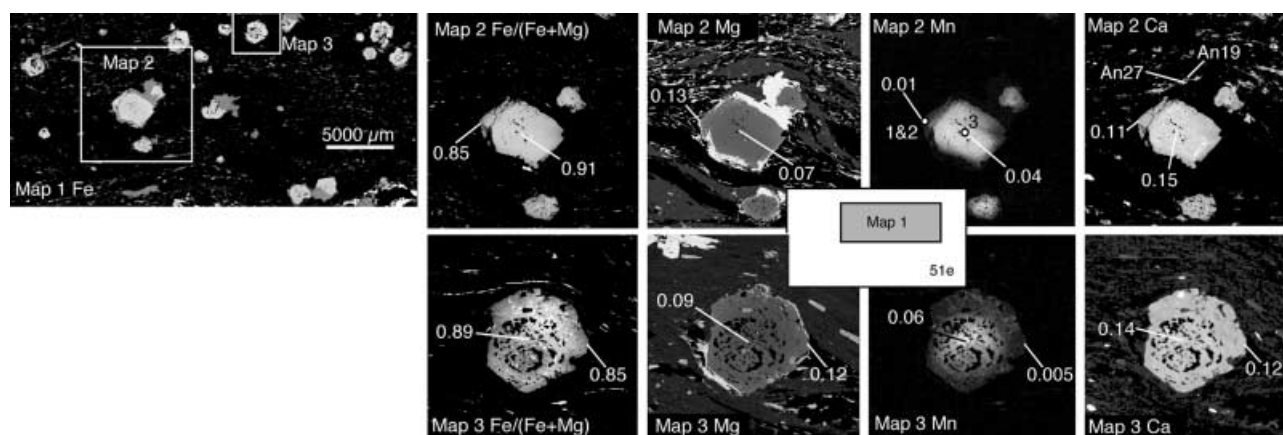
Fig. 6. X-ray maps from sample 51e for garnet and plagioclase. Location of map 1 in thin-section is indicated in line drawing at top right. In map 1, garnet is light grey and retrograde chlorite rimming garnet is medium grey. Lighter shades indicate higher concentrations. Numbered points in map 2 Mn correspond to analyses in Table 2. See text for interpretations and discussion. A colour version of this figure is available in the online version of the journal.
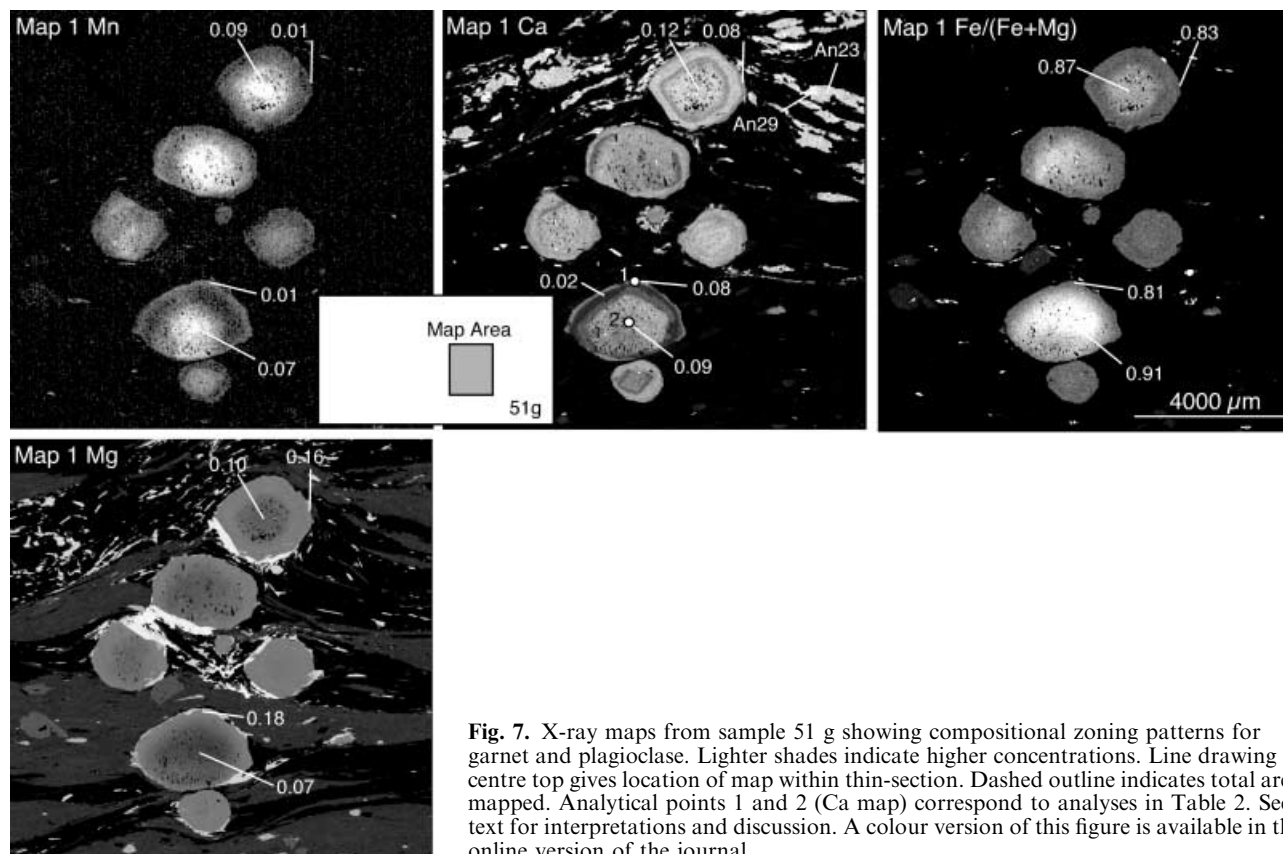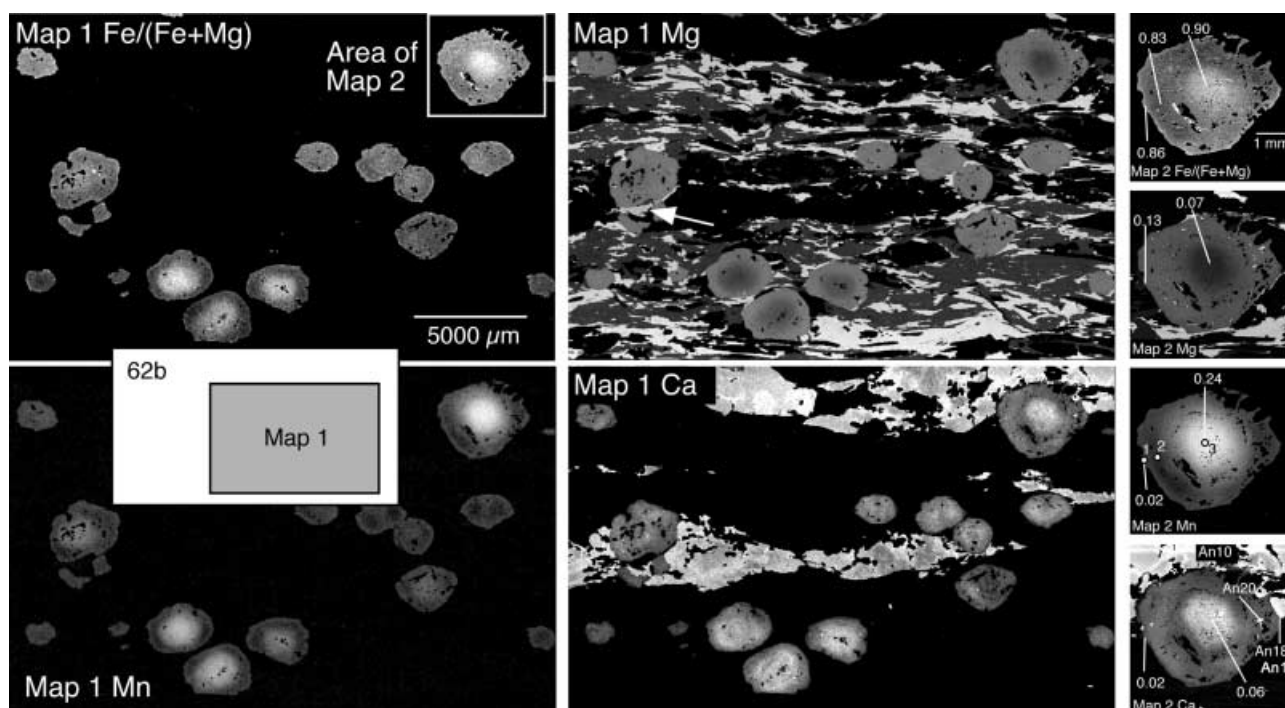

Fig. 7. X-ray maps from sample 51 g showing compositional zoning patterns for garnet and plagioclase. Lighter shades indicate higher concentrations. Line drawing at centre top gives location of map within thin-section. Dashed outline indicates total area mapped. Analytical points 1 and 2 (Ca map) correspond to analyses in Table 2. See text for interpretations and discussion. A colour version of this figure is available in the online version of the journal.

inclusions were observed within garnet from these samples, limiting the application of thermodynamic modelling and inclusion thermobarometry in determining metamorphic *P-T* paths. Plagioclase in all samples shows minor variation in core and rim compositions. Most of the matrix plagioclase in 111a preserves relatively high-Ca core compositions of $X_{An} = 0.11$–0.09 and low-Ca rims X_{An} near 0.07 (Fig. 4). However, we observed varying rim compositions of plagioclase grains that are in contact with

Fig. 8. X-ray maps for sample 62b showing compositional zoning patterns for garnet and plagioclase. Lighter shades indicate higher concentrations. Line drawing at centre left indicates location of maps within thin section. Numbered points in map 2 Mn correspond to analyses in Table 2. See text for interpretations and discussion. A colour version of this figure is available in the online version of the journal.

garnet. For example, adjacent to one garnet, plagioclase has $X_{An} = 0.11$; a second plagioclase has $X_{An} = 0.09$. In both cases, the highest Ca-content measured is where plagioclase is in contact with garnet. Moving away from the plagioclase–garnet grain boundary, X_{An} is lower by several mole percent. Similar zoning patterns were observed in the plagioclase from sample 111c, and 51e (Figs 5 & 6). The higher-Ca overgrowths observed on plagioclase adjacent to garnet are interpreted to reflect the net transfer reaction garnet + muscovite ↔ plagioclase + biotite. This reaction is strongly pressure dependent and the growth of plagioclase at the expense of garnet is likely the result of significant decompression. Biotite compositions are variable, with matrix grains preserving lower Fe/Fe + Mg ratios, whereas biotite adjacent to garnet shows higher Fe/Fe + Mg ratios (Table 4), consistent with the proposed net transfer reaction.

Staurolite-kyanite zone

Garnet within the staurolite-bearing sample (51 g), collected just above the MCT, preserves growth zoning patterns, but also shows evidence of considerable dissolution and some diffusional reequilibration of Fe, Mg and Mn across their rims (Fig. 7). Fe/Fe + Mg decreases from near 0.91 in the core to about 0.81 at the rim (Fig. 7). X_{Sps} shows a similar pattern and decreases from *c*. 0.09 in the core, to 0.005 near-rim, and then increases to near 0.01 at the rim (Fig. 7). Ca zoning is

complex and variable from garnet to garnet (Fig. 7). In general, the garnet cores show high Ca ($X_{Grs} = 0.13$) that decreases to $X_{Grs} = 0.12$–0.08 and then increases again at the rim ($X_{Grs} = 0.10$). Several crystals show multiple reversals in Ca zoning. Ca zoning patterns may be controlled by bulk compositional variations at the mm scale. The irregular outline of garnet crystals and the truncations of Ca zoning patterns are interpreted as dissolution features possibly associated with the prograde reaction garnet + chlorite + muscovite ↔ staurolite + biotite and/or the decompression reaction garnet + muscovite ↔ biotite + plagioclase. Davidson *et al.* (1997) described similar reaction textures.

Plagioclase zoning patterns in this zone are similar to those of the underlying garnet-zone samples. Core compositions are uniform at $X_{An} = 0.28$, whereas rim compositions are near $X_{An} = 0.24$. However, where garnet show considerable dissolution, it is common to observe plagioclase with higher Ca rims ($X_{An} = 0.29$; Fig. 7, Ca map). Biotite compositions vary such that matrix grains preserve lower Fe/Fe + Mg compositions relative to biotite that is adjacent to garnet (Table 4). These zoning patterns are consistent with the growth of plagioclase and biotite at the expense of garnet.

Kyanite-migmatite zone

Garnet from kyanite-bearing migmatites preserves variable zoning patterns that are interpreted to reflect

multiple episodes of growth, dissolution and diffusional re-equilibration. Small crystals (= 1 mm radius) have flat zoning profiles interpreted to be the result of diffusional reequilibration at relatively high temperatures. However, the largest crystal (2–3 mm radius) preserves growth zoning characteristics consistent with early garnet growth at lower metamorphic grade, and later garnet growth in the presence of melt (Fig. 8). The garnet rim is irregular and embayed, suggesting dissolution. This garnet also contains plagioclase inclusions that help constrain the reaction history of this sample.

Fe/Fe + Mg (Fig. 8) decreases from 0.90 (core) to 0.83 (near-rim), and increases to 0.86 at the rim. Mn decreases from $X_{Sps} = 0.26$ (core) to 0.01 near-rim, then increases to 0.02 at the rim. These compositional reversals are observed around the entire rim of the garnet and are consistent with garnet dissolution and retrograde diffusional reequilibration. A relatively high Ca core, $X_{Grs} = 0.06$, decreases to near 0.02, followed by a higher Ca overgrowth ($X_{Grs} = 0.04$) that decreases to $X_{Grs} = 0.02$ at the garnet rim.

The step from $X_{Grs} = 0.02$–0.04 in the garnet interior is interpreted to reflect garnet growth during melting via the continuous reaction muscovite + plagioclase ↔ garnet + K-feldspar + melt (Spear *et al.*, 1999). Similar zoning patterns of Ca in garnet are documented and discussed in other studies of partially melted rocks (Spear & Parrish, 1996; Spear & Kohn, 1996). This high-Ca step also correlates with minima in Mn and Fe/Fe + Mg. Muscovite is abundant in this sample and is interpreted to have replaced K-feldspar.

Plagioclase grains occur within leucosomes and typically show low Ca cores ($X_{An} = 0.10$–0.12) with higher Ca rims ($X_{An} = 0.17$). Plagioclase adjacent to garnet shows an increase in Ca towards the plagioclase–garnet grain boundary. As in the lower grade samples, this zoning pattern is interpreted to represent plagioclase growth during garnet dissolution. The high-Ca plagioclase inclusions within garnet ($X_{An} = 0.16$–0.21) are interpreted as early (premelting) compositions. Matrix biotite preserves lower Fe/Fe + Mg compositions than biotite adjacent to garnet (Table 4).

PEAK METAMORPHIC *P-T* ESTIMATES

We constrain peak metamorphic conditions by metamorphic mineral assemblages, the petrogenetic grids of Spear & Cheney (1989) and Spear *et al.* (1999), and near-rim thermobarometry calculated with Program Thermobarometry v.2 (Spear *et al.*, 1991; updated 1999). All reactions are drawn assuming $P_{H_2O} = P_t$ (Fig. 9). Although graphite is present in some samples, the aluminium-silicate and melting reactions that were used to constrain *P–T* estimates are fluid absent, and, thus, are not affected by uncertainties of water activity.

Thermobarometry cannot be applied uncritically in medium- to high-grade pelitic rocks (Florence & Spear,

1991; Frost & Chacko, 1989; Kohn & Spear, 1991, 2000; Robinson, 1991; Spear, 1991, 1993; Spear & Florence, 1992; Spear & Parrish, 1996; Davidson *et al.*, 1997; Vannay & Grasemann, 1998). The processes of intergranular diffusion and retrograde net transfer reactions can severely modify rim mineral compositions and render thermobarometric calculations meaningless (Kohn & Spear, 2000). However, the use of large area and detailed X-ray maps allowed us to better interpret and select the garnet, biotite and plagioclase compositions that most closely represent peak metamorphic compositions.

The stability field for the interpreted equilibrium mineral assemblages and *P-T* estimates from several different thermobarometers are presented in Fig. 9. Although there is considerable scatter in pressure estimates from the different calibrations, for any one calibration pressure estimates are remarkably similar. Sample 51 g is an exception. Results from thermobarometry are generally consistent with the interpreted equilibrium mineral assemblage (Fig. 9). We emphasize that Fig. 9 shows several different calibrations of the same mineral equilibria, and that the scatter in pressure estimates represents different calibrations and activity models. Table 5 presents a summary of results for the different mineral equilibria and calibrations. Barometers from Powell & Holland (1988), and Hodges & Crowley (1985) yield pressures 2–3 kbar lower than the Hoisch (1990) calibrations. The GASP barometer of Koziol (1989) yields the highest pressures.

Analytical uncertainties for thermobarometry are typically on the order of ± 5 °C, and 0.25–0.5 kbar (Kohn & Spear, 1991). However, the geological uncertainty associated with choosing the most appropriate mineral compositions far outweigh any analytical imprecision. Kohn & Spear (1991) estimate relative uncertainties for barometry at ± 0.23 to ± 0.89 kbar. These estimates vary depending upon zoning complexity, reaction history and geobarometer calibration. Based upon the complex zoning and reaction histories documented in these samples, relative uncertainties in the thermobarometry are estimated at ± 25 °C, ± 1 kbar. Although the most accurate thermobarometer calibrations are unknown, the results from all calibrations yield relatively high pressures that are consistent with metamorphism at depths between 35 and 50 km. To compare the relative *P-T* differences between samples the results are presented from the garnet-biotite thermometer of Ferry & Spear (1978) with Berman's (1990) garnet mixing model, and the geobarometers of Hoisch (1990). These calibrations are internally consistent, and applicable to all the samples from this study.

Garnet zone

Garnet-biotite thermometry for samples 111a, 111c, and 51e yields nearly identical temperatures of 660, 670 and 640 °C (at 11 kbar), respectively. The calculated
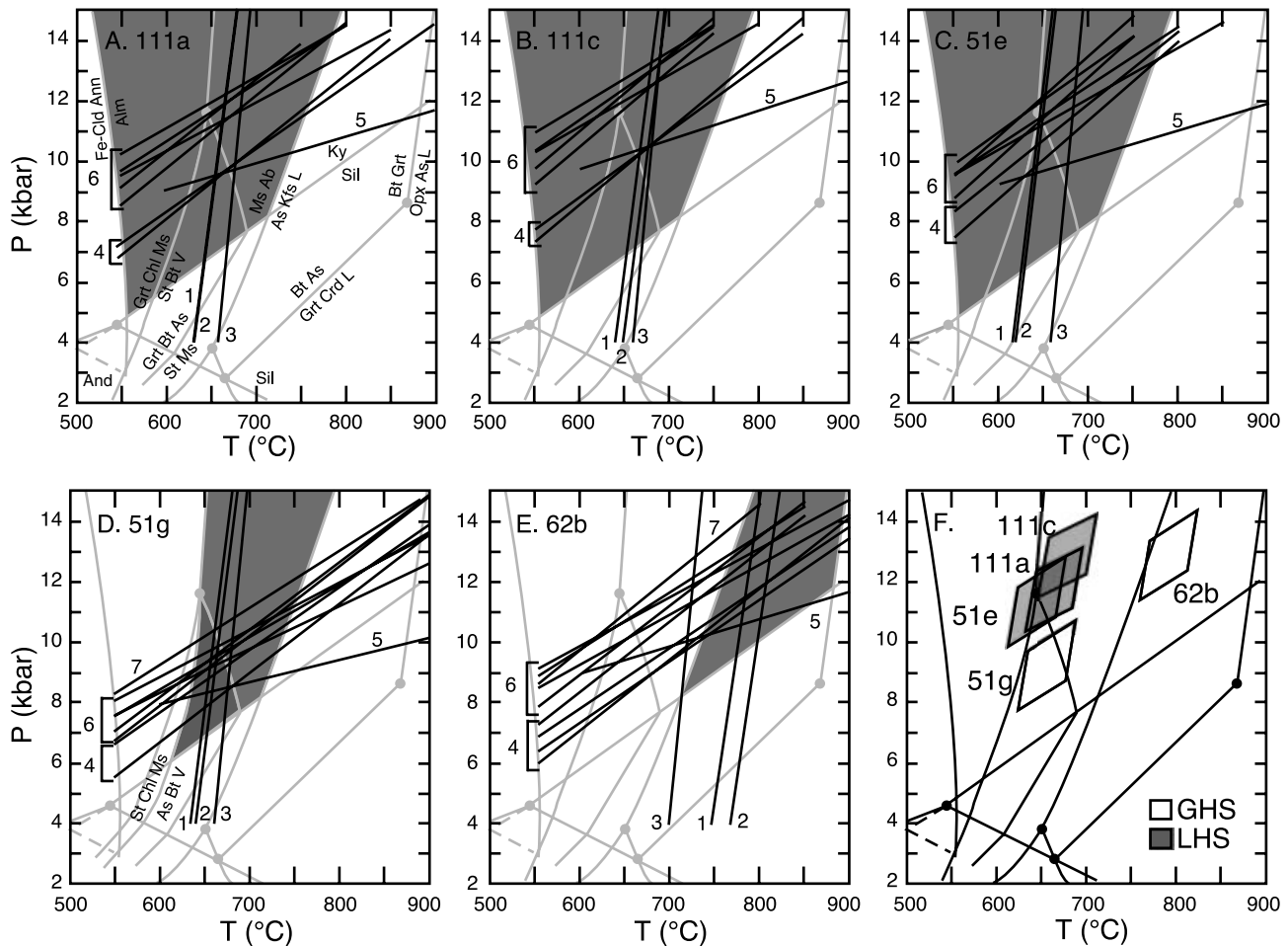
Fig. 9. Thermobarometric results for samples from the Lesser Himalayan rocks (a) 111a (b) 111c (c) 51e, and the Greater Hima-layan sequence (d) 51 g, and (e) 62b. Shaded area indicates the approximate stability region of the observed mineral assemblage. Numbers correspond to different calibrations: (1) Ferry & Spear (1978) (2) Patiño-Douce *et al.* (1993) (3) Holdaway *et al.* (1997) (4) Hodges & Crowley (5) Powell & Holland (6) Hoisch (1990), and (7) Koziol (1989). (f) Summary diagram illustrates average *P-T* conditions based upon calibrations 1 and 6, assuming an error of ± 25 °C, ± 1 kbar.

Table 5. Geobarometer calibrations and mineral equilibria.

Calibration	111a*	111c*	51e*	51g*	62b**
H&C[1] (4)					
GPMB(Fe)[2]	9.5	9.9	10.7	8.7	11.4
GPMQ(Fe)	9.5	9.8	10.0	7.8	11.8
GASP	na	na	na	8.9	11.8
P&H[1] (5)					
GPMB	9.4	10.2	9.7	8.3	10.8
H[1] (6)					
GPMB-R6	10.9	11.7	11.4	9.0	13.0
GPMB-R5	11.0	12.0	11.2	9.1	13.1
GPMQ-R3	11.9	12.7	11.5	9.6	12.6
GPMB-R2	11.5	12.2	12.1	9.3	13.0
GPBQ-R1	11.6	12.4	12.0	9.3	13.5
K[1] (7)					
GASP	na	na	na	9.6	14.3

* Pressure estimates given at T = 650 °C, ** T = 800 °C.

1. Calibrations: H&C, Hodges & Crowley (1985); P&H, Powell & Holland (1988); H, Hoisch (1990); K, Koziol (1989). Numbers in parentheses correspond to equilibria lines shown in Fig. 9.

2. Mineral Abbreviations: G, garnet; P, plagioclase; M, muscovite; B, biotite; Q, quartz; A, aluminium-silicate.

pressure estimates (at 650 °C) were 11–12 kbar for 111a, near 12 kbar for 111c, and 11–12 kbar for 51e. All calculations used near-rim garnet compositions, matrix biotite and rim compositions from matrix plagioclase. The zoning patterns in 111a and 111c show little evidence for modification of garnet rim compositions through diffusion or net transfer reactions. However, sample 51e shows evidence of significant dissolution and replacement by chlorite making the selection of a rim composition more difficult. The use of X-ray maps allowed us to recognize a relict garnet rim composition little affected by dissolution (Fig. 6), for sample 51. Based upon these samples, the peak metamorphic *P-T* conditions for rocks just below the MCT were estimated at *c.* 650 °C, 11–12 kbar. The interpreted equilibrium mineral assemblage for all three samples is garnet-biotite-muscovite-plagioclase-quartz, consistent with the thermobarometric estimates (Fig. 9).

Staurolite-kyanite zone

Garnet-staurolite-kyanite-sillimanite assemblages immediately overlie the MCT. The occurrence of kyanite and irregular, embayed staurolite grains suggests temperatures above the reaction St + Chl + Ms ↔ Ky + Bt + H_2O. The high Ca rims preserved on many of the garnet in this zone roughly correspond with inclusion free rims and are interpreted to reflect a second episode of garnet growth associated with the staurolite dissolving reaction St + Ms ↔ Grt + Ky + Bt. Based upon the mineral textures and chemical zoning, the equilibrium mineral assemblage for this sample is interpreted to be Grt + Ky + Bt. Thermobarometry estimates from sample 51 g yield approximately 650 °C at 9 kbar, and were calculated using garnet rim, matrix biotite and matrix plagioclase rim compositions. These results are generally consistent with either a peak assemblage of Ky + Bt, or Grt + Ky + Bt, depending upon the chosen calibration. We emphasize that several studies show that thermobarometry in staurolite–bearing rocks often yields temperatures significantly lower than is required for the observed mineral assemblage. These low temperatures reflect modification of the garnet rim composition through garnet dissolution via the staurolite–producing reaction and diffusional re-equilibration (Florence & Spear, 1993; Spear, 1993). According to Florence & Spear (1993), the peak metamorphic temperatures could be 50–75 °C higher than calculated. Furthermore, the pressure estimates for this sample are not in accord with pressures from samples collected tens of metres below and about 2 km above. Given the considerable amount of dissolution and diffusion of Fe, Mg and Mn in these garnet, and the variable Ca zoning (Fig. 7), it is very unlikely that the calculated *P–T* estimates for sample 51 g accurately reflect the peak metamorphic conditions.

Kyanite–migmatite zone

Kyanite-bearing migmatites begin *c.* 500 m above the MCT and continue up to the Kakhtang Thrust. The occurrence of kyanite + melt constrains the *P-T* conditions to be > *c.* 700 °C, 8 kbar (Fig. 9; Davidson *et al.*, 1997). These *P–T* estimates are minima based upon the fluid–absent reactions kyanite = sillimanite and muscovite + plagioclase ↔ kyanite + K-spar + melt (Spear *et al.*, 1999). Thermobarometry yields *c.* 800 °C at 12–13 kbar. These results are consistent with the peak mineral assemblage, except no K-spar was observed in these samples. K-spar may have been consumed during cooling and crystallization of the melt via the continuous reaction Grt + K-spar + melt ↔ Bt + Al_2SiO_5, and/or the discontinuous reaction Al_2SiO_5 + K-spar + melt ↔ Ms + Pl + Qtz (Spear *et al.*, 1999). Alternatively, melting may be the result of fluid infiltration and melting via the reaction

Ms + Ab + H_2O ↔ Al_2SiO_5 + melt. The preservation of growth zoning patterns in the largest garnet crystals suggests a short residence time at elevated temperatures, and rapid cooling.

### Discussion of peak estimates of pressure and temperature

Most remarkable is the similarity in pressures across the MCT. Pressure estimates in the footwall are 11–13 kbar based upon the thermobarometry in sample 111a, 111c and 51e. The minimum pressure at the base of the hanging wall is 8 kbar based upon the assemblage kyanite + melt, and thermobarometry indicates higher pressures of 12–13 kbar. Thus, there is a metamorphic field gradient with temperature increasing from the footwall into the hanging wall, but there is no measurable break in pressure across the MCT (Fig. 9). This is consistent with top-to-the-south shearing distributed across a wide zone (the MCTZ) as opposed to having the displacement occur along a single discrete plane such as the MCT. The kyanite-bearing leucogranites and migmatites clearly have a deep crustal origin. The high-Ca overgrowths observed in sample 111a, and 111c (and sample 43 from Davidson *et al.*, 1997) are consistent with garnet growth after a large increase in pressure.

Regardless of which geobarometer calibration is chosen, pressure estimates are generally consistent and indicate exhumation of the MCT and adjacent rocks from lower crustal depths. Assuming an average crustal density of 2.8 g cm^{-3}, the pressure estimates based on Hoisch (1990) correspond to depths of 40–45 km. Pressure estimates based on Hodges & Crowley (1985) and Powell & Holland (1988) correspond to depths of 35–43 km. Cross sections from Grujic *et al.* (2002), and Hauck *et al.* (1998) show the MCT projecting approximately 200 km north at a dip of 10–15°. Seismic interpretations from Hauk *et al.* (1998; Fig. 7) show that the MCT/MHT can be reasonably traced to depths of 45–50 km and may extend even deeper (about 55 km) before flattening out. Assuming that the dip angle of the MCT/MHT has not changed significantly during the last 25 Myr, then the MCT/MHT has been exhumed laterally from under Tibet by a minimum of *c.* 150 km.

U∕PB GEOCHRONOLOGY

Analytical methods

U-Pb analyses were conducted on single grains or small numbers of grains of monazite and∕or xenotime separated from samples using standard mineral separation techniques. U-Pb analytical methods used were similar to those described in Parrish *et al.* (1987), using a mixed ^{205}Pb-^{233}U-^{235}U spike, and a VG 354 mass spectrometer equipped with a Daly photomultiplier ion counting detector and WARP filter. All relevant sources of error were incorporated and uncertainties were derived in a manner similar to that described in Roddick *et al.* (1987). Some of the larger crystals required multiple dissolution steps with both HCl and HNO$_3$ acids. These crystals were
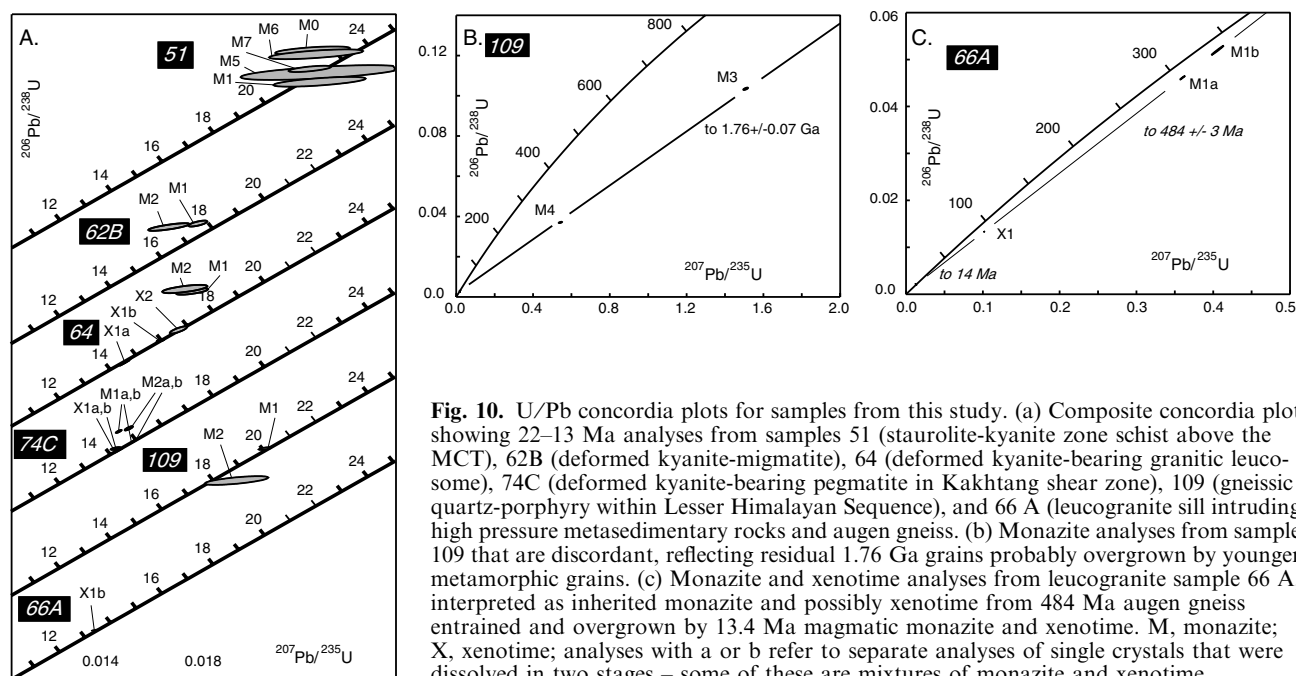
Fig. 10. U/Pb concordia plots for samples from this study. (a) Composite concordia plot showing 22–13 Ma analyses from samples 51 (staurolite-kyanite zone schist above the MCT), 62B (deformed kyanite-migmatite), 64 (deformed kyanite-bearing granitic leucosome), 74C (deformed kyanite-bearing pegmatite in Kakhtang shear zone), 109 (gneissic quartz-porphyry within Lesser Himalayan Sequence), and 66 A (leucogranite sill intruding high pressure metasedimentary rocks and augen gneiss. (b) Monazite analyses from sample 109 that are discordant, reflecting residual 1.76 Ga grains probably overgrown by younger metamorphic grains. (c) Monazite and xenotime analyses from leucogranite sample 66 A, interpreted as inherited monazite and possibly xenotime from 484 Ma augen gneiss entrained and overgrown by 13.4 Ma magmatic monazite and xenotime. M, monazite; X, xenotime; analyses with a or b refer to separate analyses of single crystals that were dissolved in two stages – some of these are mixtures of monazite and xenotime.

analyzed separately and listed in Table 6 with analysis identifiers *a* and *b*, referring to the first partial dissolution and the final (complete) dissolution, respectively. Data are tabulated in Table 6 and shown in an array of concordia diagrams in Fig. 10. U and Pb blanks during the course of the work ranged from 0 to 1 pg U and 3–15 pg Pb. Analyses lying above the concordia curve are exclusively monazite crystals or components and contain an excess amount of ^{206}Pb from preferential incorporation of initial ^{230}Th (see Parrish, 1990); in such cases, the ^{207}Pb/^{235}U age is used in the age interpretation.

Results

Lesser Himalayan Sequence

A quartz-feldspar gneissic rock occurs as a sheet-like, structurally concordant body several hundred metres structurally below the MCT (Gansser, 1983), about 30 km west of Tashigang. Thimm *et al.* (1999) reported a preliminary 20 Ma date on monazite from sample 109 of this unit, full data are shown in Fig. 10(a,c). This gneiss was deformed and metamorphosed under greenschist facies metamorphic conditions. Monazite of both Proterozoic and Miocene age (*c.* 20 Ma) occur in this sample, the latter being metamorphic in origin. Zircon from this sample implies an age between 1.76 and 1.84 Ga, and are in part inherited (unpublished data), but monazite colinear analyses argue for a magmatic crystallization age of 1.76 ± 0.07 Ga and a growth age of metamorphic crystals/overgrowths between 18 and 20 Ma, the latter 20.0 ± 0.2 age being the most precise. The date implies that the deformation at greenschist facies conditions (over 400 °C) in the footwall was also related to the south directed thrusting that was underway by 22 Ma, and continued until perhaps 14 Ma or younger (see below).

Greater Himalayan Sequence

A biotite schist (51 g), just above the MCT, contains metamorphic monazite with abundant visible inclusions. Multiple analyses yielded an age of *c.* 22 ± 1 Ma (Fig. 10), although the high common Pb content of the crystals gives increased uncertainty. This growth age is in line with other reported ages that were interpreted to reflect thrusting across the MCTZ (Hodges, 2000 and references therein).

Monazite and xenotime dates from kyanite-bearing leucosomes and migmatites (samples 62b & 64) in close proximity to the MCT have measured ages from 18 to 14.5 Ma (Fig. 10). Xenotime is generally somewhat younger than monazite, possibly the result of being less retentive of Pb than monazite; alternatively, U-loss in monazite could produce slightly excessive monazite ages. The data are complicated in detail and may also reflect progressive crystallization of these mineral phases over several million years during both moderate pressure conditions and exhumation. The monazite grains are interpreted as igneous in origin and the ages are interpreted as crystallization ages. The distinctive magmatic nature of most of the crystals analyzed implies that the high–pressure (10–13 kbar) metamorphism and anatexis occurred during the 14–18 Ma interval.

Sample 66 A is a 1–2 km thick leucogranite sill near Tashigang that intrudes both high-pressure metasedimentary rock and augen gneiss. Large, euhedral monazite and xenotime single crystals were analyzed, yielding evidence for early Palaeozoic crystallization (Fig. 10). Xenotime was dissolved in two stages, with a

Th-enriched possibly monazite-bearing component providing additional evidence for inheritance and a Th-poor xenotime component (the last to fully dissolve) yielding a concordant age of 13.4 ± 0.2 Ma. The analyses form a colinear array (MSWD 0.7) with upper intercept of 484 ± 3 Ma which records the age of formerly magmatic monazite inherited from local augen gneiss. Importantly, this inherited age confirms an early Palaeozoic age of the augen gneiss proximal to the MCT in this region. All ages are interpreted as crystallization ages. The presence of top-to-the-south, melt–filled shear bands within the sill (Fig. 3d), indicates melt-present deformation within the GHS at 13.5 Ma.

Below the Kahktang Thrust at location 74 (Fig. 1), south–directed shearing disrupts pegmatites and produces boudinage. These pegmatites contain kyanite and are associated with kyanite migmatite schists. One of the boudinaged pegmatites (sample 74C) contained igneous monazite and xenotime that were analyzed in two separate dissolution stages, yielding crystallization ages from 15.0 to 14.2 Ma. These data are consistent with high–pressure metamorphism at 15–14 Ma.

METAMORPHIC *P-T-t* PATHS

High-variance assemblages, diffusional modification of growth zoning, retrograde net transfer reactions, and a lack of suitable inclusions within garnet hamper the reconstruction of the prograde metamorphic evolution for both the LHS and GHS. However, the peak metamorphic conditions are relatively well constrained, as is part of the retrograde path (Davidson *et al.*, 1997). For the uppermost Lesser Himalayan rocks, we can infer a clockwise *P-T* loop of early heating and compression based upon the occurrence of high-Ca rims, syn- to intertectonic cores in garnet with prograde zoning, and numerical simulations (Beaumont *et al.*, 2001). However, the exact nature and slope of their prograde paths is unconstrained and is not shown in Fig. 11. Within the GHS, a few samples show relict staurolite as inclusions within garnet and as fragments within leucosomes, indicating heating, and possibly compression from the staurolite stability field into the kyanite + melt field (Davidson *et al.*, 1997).

The kyanite-bearing melts immediately above the MCT are inferred to have cooled from peak temperatures during the underthrusting of the cooler Lesser Himalayan rocks and then experienced decompression to near 5 kbar (Fig. 11). This inference of cooling and decompression is suggested by the lack of sillimanite associated with the leucosomes. Kyanite-sillimanite bearing leucogranites at higher structural levels (sample 74) are inferred to have decompressed through the sillimanite-melt field and then cooled; however, peak *P-T* estimates for this sample are only constrained by the assemblage Ky + melt. This path is based upon the replacement of kyanite by sillimanite, the association of abundant
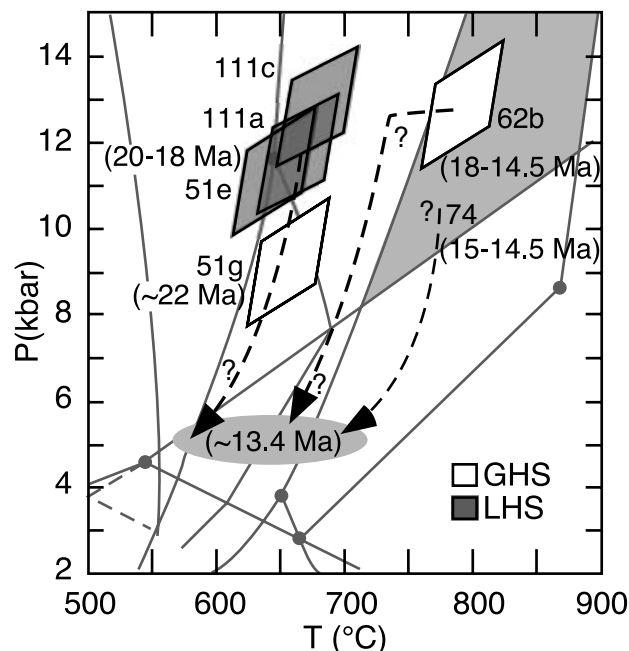
Fig. 11. Summary *P-T-t* diagram showing monazite/xenotime ages and estimated peak metamorphic conditions for the uppermost Lesser Himalayan rocks (111a, c, 51e) and the lower Greater Himalayan sequence from the MCT (51 g, 62b) up to the Kakhtang Thrust (74c). Retrograde conditions based upon our data and results from Davidson *et al.* (1997). Reactions as on Fig. 9(a).

sillimanite near bodies of leucogranite, and the dissolution of garnet to grow plagioclase and biotite ± sillimanite. Davidson *et al.* (1997) documented similar decompression reaction textures for the GHS near the Kakhtang thrust in central Bhutan and estimated that the final emplacement of leucogranites occurred at *c.* 5 kbar. Monazite from kyanite migmatites are dated at 18–16 Ma; monazite from leucosome-filled shear bands are as young as *c.* 13 Ma. Thus, we infer decompression from 35 to 45 km depth to near 18 km depth in 3–5 Myr, yielding exhumation rates of 3–9 mm yr^{-1}.

DISCUSSION & CONCLUSIONS

Building upon the previous work of Swapp & Hollister (1991), Grujic *et al.* (1996, 2002) and Davidson *et al.* (1997), and the new metamorphic, geochronological and structural data documented in this work, the following conclusions and interpretations are made about the metamorphic, plutonic and deformational history of the MCTZ in eastern Bhutan:
(1) Peak metamorphic pressures are uniform across the MCT at 11–13 kbar, suggesting the footwall and hanging wall were juxtaposed at depths corresponding to these pressures. These data are not consistent with major syn- to postmetamorphic thrusting of the GHS over the LHS across the MCT.

(2) Peak temperatures increase from 650 to 675 °C within the uppermost Lesser Himalayan sequence to 750–800 °C, some 500 m above the trace of the MCT. Metamorphic temperatures of 750–800 °C are inferred to continue up to the out-of-sequence Kakhtang thrust based upon the continued presence of kyanite-migmatites.

(3) Decompression from 10 to 13 kbar to near 5 kbar (Swapp & Hollister, 1991; Davidson *et al.,* 1997) at high temperature is recorded within the hanging wall of the MCT and some evidence of decompression is detected in the footwall.

(4) Penetrative top-to-the-south thrusting occurred from at least 2 km below the MCT up to the STD (Grujic *et al.*, 1996, 2002) and postdates the high-pressure metamorphism. Within the GHS, top-to-the-north shear bands, boudinaged kyanite, and symmetrical, melt-filled pressure shadows around garnet indicate a component of late pure shear and late north-directed shearing (Grujic *et al.*, 1996, 2002).

(5) Multiple generations of crosscutting leucogranite and leucotonalite pods, dykes, and sills range from strongly deformed, to relatively undeformed, and leucosomes fill south-verging and north-verging conjugate shear bands. This indicates that melt was present during deformation and decompression (Davidson *et al.*, 1997).

(6) Penetrative thrust deformation and metamorphism was underway by at least 22–20 Ma within the Lesser Himalayan rocks and the lowermost Greater Himalayan rocks.

(7) Kyanite-bearing migmatites were formed at 18–16 Ma.

(8) Below the Kakhtang thrust, the syn-tectonic emplacement of leucogranite continued from *c.* 18 Ma until *c.* 13 Ma.

(9) Exhumation rates from the lower crust to the middle crust for rocks from the Main Central Thrust Zone were 3–9 mm yr^{-1}.

Although there is little question that south-directed shearing postdates peak metamorphism, there is no measurable inverted pressure gradient across the MCT. Similar results and interpretations were reported for the Sutlej valley region of NW India. Vannay & Grasemann (1998), and Vannay *et al.* (1999) documented inverted temperature gradients, but relatively uniform metamorphic pressures across the entire GHS of the NW Himalaya. They proposed that such results are inconsistent with a postmetamorphic inversion of the metamorphic isograds by folding, simple shear, or thrusting. Vannay & Grasemann (2001) proposed a model of extrusion accommodated by general shear with a large component of pure shear to explain their observations.

Grujic *et al.* (1996, 2002) presented a model of ductile extrusion for the Bhutan Himalaya, whereby south-directed channel-flow (the MCTZ) results in the simultaneous underthrusting of India and the north-directed extension along the South Tibetan Detach-ment. Channel flow, driven by a pressure gradient, can be triggered when the viscosity of the rocks in the GHS attains a low threshold value (e.g. at high temperature and partial melting; Beaumont *et al.*, 2001).

The simultaneous operation of the MCTZ and the STDZ is well documented and many previous workers have proposed an extruding wedge for the Himalayas (either rigid: Burchfiel & Royden, 1985; Kündig, 1989; Burchfiel *et al.*, 1992; Hodges *et al.*, 1993; or ductile: Grujic *et al.*, 1996; Davidson *et al.*, 1997). These studies show cross sections with the MCT and the STD intersecting at depth. However, seismic interpretations from the INDEPTH project, north of Bhutan, show no such intersection (Makovsky *et al.*, 1996; Hauck *et al.*, 1998). Based upon this interpretation for the geometry of the MHT-STD system, we present a conceptual model for the exhumation of the MCT from lower crustal depths.

Figure 12 presents a cartoon incorporating the major *P-T-t-D* information into a model of channel flow based upon the work of Grujic *et al.* (1996, 2002) and Beaumont *et al.* (2001). This model focuses upon the exhumation of the lower half of the MCTZ, and does not incorporate the out-of-sequence thrusting associated with the Kakhtang thrust. Figure 12(a) illustrates a south vergent velocity gradient across an early MCTZ. The LHS and GHS were most likely underthrust to lower crustal depths along a precursor to the modern MCTZ. If this deformation zone widened or progressively moved to the south through in-sequence thrusting, then the uppermost levels of the LHS would eventually be incorporated into the MCTZ. The large ellipses represent the uncertainty in the early prograde *P-T-t* history of the samples for the uppermost LHS (111 samples) and the lowermost part the GHS (samples 51 g & 62b).

Maximum depths were reached at similar times, but the lateral distance separating the samples could be significant (Fig. 12b). Back-flow within the MCTZ has initiated, resulting in a parabolic velocity profile yielding top-to-the-north shear at the top of the MCTZ, and top-to-the-south shear across the base, with respect to a fixed reference frame in the hanging wall of the STD. This extrusion model predicts a variable displacement field within the extruding channel, such that material in the centre of the channel flows faster than material along the sides of the channel. Back-flow is the process responsible for the inversion of the metamorphic temperature gradient across the MCT. The temperature inversion across the MCTZ and GHS is thus a dynamic effect introduced during extrusion within the channel and exhumation of both the hanging wall and footwall of the MCT (see also Beaumont *et al.*, 2001). No inverted pressure gradient is produced due to the flattening of the shear zone at depth.

Extrusion of channel material towards the surface brings material out from underneath Tibet up to middle and upper crustal levels (Fig. 12c,d). Ductile
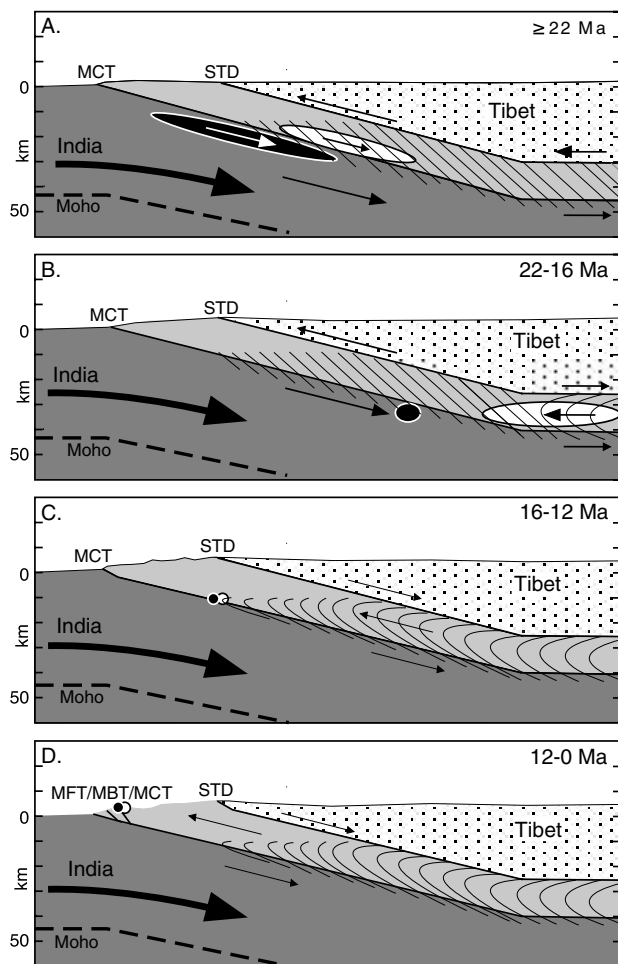
Fig. 12. Cartoon placing *P-T-t* data in context of a channel flow model proposed for Bhutan (Grujic *et al.*, 2002). The white ellipse represents the lower GHS; the black ellipse represents the uppermost LHS. Vertical scale ≃ horizontal scale. (a) Underthrusting across the MCTZ (hatchered area) and metamorphism of GHS and LHS underway by *c.* 22 Ma. Large ellipses correspond to poorly constrained prograde *P-T* history of samples. (b) GHS and LHS are underthrust to similar depths (35–45 km), but may be separated laterally a considerable distance. Backflow has initiated within the MCTZ producing top-to-the-north shear at top of MCTZ, and top-to-the-south shear at bottom of MCTZ. (c) Ductile backflow within the MCTZ coupled with rapid erosion is responsible for exhumation from lower crustal (35–45 km) to middle crustal (near 15 km) depths and the juxtaposition of samples from the LHS and GHS occurs somewhere between 40 km and 18 km (d) Subsequent exhumation of MCT to the surface is accomplished through channel backflow, displacement across the MFT/MBT/MHT system and erosion.

back flow is inferred to stop at middle crustal levels, at the brittle/ductile transition. Relative particle paths within the channel will depend upon local velocity in the channel, relative amounts of pure and simple shear, and variations in viscosity across the channel due to the spatial variation and amount of melt present in the channel. Somewhere between *c.* 40 km and *c.* 18 km the displacement paths of the samples from the LHS

and GHS samples converge (that is, they were juxtaposed), and were subsequently exhumed together through combined displacement along the MFT–MBT–MHT system (Fig. 12d), and concomitant surface denudation. The occurrence of kyanite-bearing leucogranites and leucosomes in the GHS implies a lower crustal origin (Fig. 12b,c); tectonic transport into the middle and upper crust during ductile extrusion is implied by the decompression metamorphic reactions (Davidson *et al.*, 1997).

SUPPLEMENTARY MATERIAL

Tables S2–S4 and S6, and colour versions of Figs 4, 5, 6, 7 and 8 are available online at http://www.blackwellpublishing.com/products/journals/suppmat/JMG/JMG445/JMG445.htm.

REFERENCES

Beaumont, C., Jamieson, R. A., Nguyen, M. H. & Lee, B., 2001. Himalayan tectonics explained by extrusion of a low-viscosity crustal channel coupled to focused surface denudation. *Nature*, **414**, 738–742.

Berman, R. G., 1990. Mixing properties of Ca-Mg-Fe-Mn garnets. *American Mineralogist*, **75**, 328–344.

Bhargava, O. N., ed., 1995. *The Bhutan Himalaya: a geological account, Special Publication 39*, p. 245, Geological Society of India, Calcutta.

Burchfiel, B. C., Chen, Z., Hodges, K. V., Liu, Y., Royden, L. H., Deng, C. & Xu, J., 1992. The South Tibetan detachment

system, Himalayan orogen: Extension contemporaneous with and parallel to shortening in a collisional mountain belt. *Geological Society of America Special Paper*, **269,** 41.

Burchfiel, B. C. & Royden, L. H., 1985. North-south extension within the convergent Himalayan region. *Geology*, **13,** 679–682.

Dasgupta, S., 1995. Jaishidanda Formation. In: *The Bhutan Himalaya: a Geological Account, Special Publication 39*, (ed. Bhargava, O. N.), pp. 79–88. Geological Survey of India, Calcutta.

Davidson, C., Grujic, D. E., Hollister, L. S. & Schmid, S. M., 1997. Metamorphic reactions related to decompression and synkinematic intrusion of leucogranite, High Himalayan Crystallines, Bhutan. *Journal of Metamorphic Geology*, **15,** 593–612.

Dietrich, V. & Gansser, A., 1981. The leucogranites of the Bhutan Himalaya (crustal anatexis versus mantle melting). *Schweizerische Mineralogische und Petrographische Mitteilungen*, **61,** 177–202.

Edwards, M. A., Kidd, W. S. F., Li, J., Yue, Y. & Clark, M., 1996. Multi-stage development of the southern Tibet detachment system near Khula Kangri: New data from Gonta La. *Tectonophysics*, **260,** 1–19.

Edwards, M. A., Pecher, A., Kidd, W. S. F., Burchfiel, B. C. & Royden, L. H., 1999. Southern Tibetan Detachment System at Khula Kangri, eastern Himalaya: a large-area, shallow detachment stretching into Bhutan? *Journal of Geology*, **107,** 623–311.

Ferry, J. M. & Spear, F. S., 1978. Experimental calibration of the partitioning of Fe and Mg between biotite and garnet. *Contributions to Mineralogy and Petrology*, **66,** 113–117.

FitzGerald, J. D. & Stünitz, H., 1993. Deformation of granitoids at low metamorphic grade. I: Reactions and grain size reduction. *Tectonophysics*, **221,** 269–297.

Florence, F. P. & Spear, F. S., 1991. Effects of diffusional modification of garnet growth zoning on P-T path calculations. *Contributions to Mineralogy and Petrology*, **107,** 487–500.

Florence, F. P. & Spear, F. S., 1993. Influences of reaction history and chemical diffusion on P-T calculations for staurolite schists from the Littleton Formation, northwestern New Hampshire. *American Mineralogist*, **78,** 345–359.

Frost, B. R. & Chacko, T., 1989. The granulite uncertainty principle: Limitations on thermobarometry in granulites. *Journal of Geology*, **97,** 435–450.

Gansser, A., 1964. *Geology of the Himalaya*. Wiley-Interscience, London.

Gansser, A., 1983. Geology of the Bhutan Himalaya. *Denkschriten der Schweizerischen Naturforschenden Gesellschaft*. Birkhauser-Verlag, Basel.

Grasemann, B., Fritz, H. & Vannay, J. C., 1999. Quantitative kinematic flow analysis of the Main Central Thrust Zone (NW Himalaya, India): implications for a decelerating strain path and the extrusion of orogenic wedges. *Journal of Structural Geology*, **21,** 837–853.

Grasemann, B. & Vannay, J. C., 1999. Flow controlled inverted metamorphism in shear zones. *Journal of Structural Geology*, **21,** 743–750.

Grujic, D., Casey, M., Davidson, C., Hollister, L., Kündig, R. & Pavlis. & Schmid, S., 1996. Ductile extrusion of the Higher Himalayan Crystalline in Bhutan: evidence from quartz microfabrics. *Tectonophysics*, **260,** 21–43.

Grujic, D., Hollister, L. S. & Parrish, R. R., 2002. Himalayan metamorphic sequence as an orogenic channel: Insight from Bhutan. *Earth and Planetary Science Letters*, **198,** 177–191.

Hand, M. & Dirks, P. H. G. M., 1992. The influence of deformation on the formation of axial-planar leucosomes and the segregation of small melt bodies within migmatitic Napperby Gneiss, central Australia. *Journal of Structural Geology*, **14,** 591–604.

Harrison, T. M., Grove, M., Lovera, O. M. & Catlos, E. J., 1998. A model for the origin of Himalayan anatexis and inverted metamorphism. *Journal of Geophysical Research*, **103,** 27,017–27,032.

Harrison, T. M., Ryerson, F. J., Le Fort, P., Yin, A., Lovera, O. & Catlos, E. J., 1997. A model for the origin of Himalayan anatexis and inverted metamorphism. *Earth and Planetary Science Letters*, **146,** E1–E7.

Hauck, M. L., Nelson, K. D., Brown, L. D., Zhao, W. & Ross, A. R., 1998. Crustal structure of the Himalayan orogen at ~90° east longitude from project INDEPTH deep reflection profiles. *Tectonics*, **17,** 481–500.

Heim, A. & Gansser, A., 1939. Central Himalaya. Geological observations of the Swiss expedition, 1939. *Denkschriften der Schweizerischen Naturforschenden Gesellschaft*, **73,** 1–245.

Hodges, K. V., 2000. Tectonics of the Himalaya and southern Tibet from two perspectives. *Geological Society of America Bulletin*, **112,** 324–350.

Hodges, K. V., Burchfiel, B. C., Royden, L. H., Chen, Z. & Xu, J., 1993. The metamorphic signature of contemporaneous extension and shortening in the central Himalayan orogen: Data from the Nyalam transect, southern Tibet. *Journal of Metamorphic Geology*, **11,** 721–737.

Hodges, K. V. & Crowley, P., 1985. Error estimation and empirical geothermobarometry for pelitic systems. *American Mineralogist*, **70,** 702–709.

Hoisch, T. D., 1990. Empirical calibration of six geobarometers for the mineral assemblage quartz + muscovite + biotite + plagioclase + garnet. *Contributions to Mineralogy and Petrology*, **104,** 225–234.

Holdaway, M. J., Mukhopadhyay-Biswajit, Dyar, M. D., Guidotti, C. V. & Dutrow. B. L., 1997. Garnet-biotite geothermometry revised, new Margules parameters and a natural specimen data set from Maine. *American Mineralogist*, **82,** 582–595.

Hubbard, M. S., 1989. Thermobarometric constraints on the thermal history of the Main Central thrust zone and Tibetan slab, eastern Nepal Himalaya. *Journal of Metamorphic Geology*, **7,** 19–30.

Hubbard, M. S., 1996. Ductile shear as a cause of inverted metamorphism: Example from the Nepal Himalaya. *Journal of Geology*, **194,** 493–499.

Jain, A. K. & Manickavasagam, R. M., 1993. Inverted metamorphism in the intracontinental ductile shear zone during Himalayan collision tectonics. *Geology*, **21,** 407–410.

Jamieson, R. A., Beaumont, C., Hamilton, J. C. & Fullsack, P., 1996. Tectonic assembly of inverted metamorphic sequences. *Geology*, **9,** 839–842.

Kohn, M. J., Catlos, E. J., Ryerson, F. J. & Harrison, T. M., 2001. Pressure-temperature-time path discontinuity in the Main Central Thrust zone, central Nepal. *Geology*, **29,** 571–574.

Kohn, M. J. & Spear, F. S., 1991. Error propagation for barometers: 2. Application to rocks. *American Mineralogist*, **76,** 138–147.

Kohn, M. J. & Spear, F. S., 2000. Retrograde net-transfer reaction insurance for pressure-temperature estimates. *Geology*, **28,** 1127–1130.

Koziol, A., 1989. Recalibration of the garnet-plagioclase-Al$_2$SiO$_5$-quartz (GASP) geobarometer and application to natural parageneses. *EOS Transactions American Geophysical Union*, **70,** 493.

Kündig, R., 1989. Domal structures and high-grade metamorphism in the Higher Himalayan crystalline, Zanskar region, north-west Himalaya, India. *Journal of Metamorphic Geology*, **7,** 43–56.

LeFort, P., 1975. Himalayas: The collided range. Present knowledge of the continental arc. *American Journal of Science*, 275-A, 1–44.

Makovsky, Y., Klemperer, S. L., Huang, L., Lu, D. & Project INDEPTH, Team, 1996. Structural elements of the southern Tethyan Himalaya crust from wide-angle seismic data. *Tectonics*, **15,** 997–1005.

Parrish, R. R., 1990. U-Pb dating of monazite and its application to geological problems. *Canadian Journal of Earth Sciences*, **27,** 1431–1450.

Parrish, R. R., Roddick, J. C., Loveridge, W. D. & Sullivan, R. W., 1987. Uranium-Lead analytical techniques at the geochronology laboratory. *Geological Survey of Canada Paper*, **87–2,** 3–7.

Passchier, C. W. & Trouw, R. W. J., 1996. *Microtectonics*. Springer-Verlag, New York.

Patiño-Douce, A. E., Johnston, A. D. & Rice, J. M., 1993. Octahedral excess mixing properties in biotite: a working model with applications to geobarometry and geothermometry. *American Mineralogist*, **78,** 113–131.

Pêcher, A., 1989. The metamorphism in the central Himalaya. *Journal of Metamorphic Geology*, **7,** 31–41.

Powell, R. & Holland, T. J. B., 1988. An internally consistent thermodynamic database with uncertainties and correlations: 3. Applications to geobarometry, worked examples, and a computer program. *Journal of Metamorphic Geology*, **6,** 173–204.

Ray, S. R., 1995. Lateral variation in geometry of thrust planes and its significance, as studied in the Shumar allochthon, Lesser Himalayas, eastern Bhutan. *Tectonophysics*, **249,** 125–139.

Ray, S. R., Bandyopadhyay, B. K. & Razdan, R. K., 1989. Tectonics of a part of the Shumar allochthon in eastern Bhutan. *Tectonophysics*, **169,** 51–58.

Robinson, P., 1991. The eye of the petrographer, the mind of the petrologist. *American Mineralogist*, **76,** 1781–1810.

Roddick, J. C., Loveridge, W. D. & Parrish, R. R., 1987. Precise U/Pb dating of zircon of the sub-nanogram. *Pb Level; Chemical Geology (Isotope Geoscience Section)*, **66,** 111–121.

Schelling, D. & Arita, K., 1991. Thrust tectonics, crustal shortening, and the structure of the far eastern Nepal Himalaya. *Tectonics*, **10,** 851–862.

Spear, F. S., 1991. On the interpretation of peak metamorphic temperatures in light of garnet diffusion during cooling. *Journal of Metamorphic Geology*, **9,** 379–388.

Spear, F. S., 1993. Metamorphic phase equilibria and pressure-temperature-time paths. *Washington D.C., Mineralogical Society of America Monograph*, **1,** 799.

Spear, F. S. & Cheney, J. T., 1989. A petrogenetic grid for pelitic schists in the system SiO_2-Al_2, O_3-FeO-MgO-K_2O–H_2O. *Contributions to Mineralogy and Petrology*, **101,** 149–164.

Spear, F. S. & Florence, F. P., 1992. Thermobarometry in granulites: Pitfalls and new approaches. *Journal of Precambrian Research*, **55,** 209–241.

Spear, F. S. & Kohn, M. J., 1996. Trace element zoning in garnet as a monitor of crustal melting. *Geology*, **24,** 1099–1102.

Spear, F. S., Kohn, M. J. & Cheney, J. T., 1999. P-T paths from anatectic pelites. *Contributions to Mineralogy and Petrology*, **134,** 17–32.

Spear, F. S. & Parrish, R. R., 1996. Petrology and cooling rates of the Valhalla Complex, British Columbia, Canada. *Journal of Petrology*, **37,** 733–765.

Spear, F. S., Peacock, S. M., Kohn, M. J., Florence, F. P. & Menard, T., 1991. Computer programs for petrologic P-T-t path calculations. *American Mineralogist*, **76,** 2009–2012.

Swapp, S. M. & Hollister, L. S., 1991. Inverted metamorphism within the Tibetan slab of Bhutan: evidence for a tectonically transported heat-source. *Canadian Mineralogist*, **29,** 1019–1041.

Thimm, K. A., Parrish, R. R., Hollister, L. S., Grujic, D., Klepeis, K. & Dorji, T., 1999. New U-Pb data from the MCT and Lesser and Greater Himalayan sequences in Bhutan. *European Union of Geosciences conference abstracts;. EUG*, **10,** 57.

Vannay, J. C. & Grasemann, B., 1998. Inverted metamorphism in the High Himalaya of Himachal Pradesh (NW India): phase equilibria versus thermobarometry. *Schweizerische Mineralogische und Petrographische Mitteilungen*, **78,** 107–132.

Vannay, J. C. & Grasemann, B., 2001. Himalayan inverted metamorphism and syn-convergence extension as a consequence of a general shear extrusion. *Geological Magazine*, **138,** 253–276.

Vannay, J. C., Sharp, Z. D. & Graseman, B., 1999. Himalayan inverted metamorphism constrained by oxygen isotope thermometry. *Contributions to Mineralogy and Petrology*, **137,** 90–101.

Wu, C., Nelson, K. D., Wortman, G., Samson, S., Yue, Y., Li, J., Kidd, W. S. F. & Edwards, M. A., 1998. Yadong cross structure and South Tibetan Detachment in the east central Himalaya (89°–90°E). *Tectonics*, **17,** 28–45.

Zhao, W. & Project INDEPTH, Team, 1993. Deep seismic-reflection evidence for continental underthrusting beneath southern Tibet. *Nature*, **366,** 557–559.